



## Thermal and kinematic modeling of bedrock and detrital cooling ages in the central Himalaya

I. D. Brewer<sup>1</sup> and D. W. Burbank<sup>2</sup>

Received 7 July 2004; revised 17 March 2006; accepted 1 June 2006; published 30 September 2006.

[1] We introduce a new method that convolves detrital mineral cooling ages with digital elevation models to test numerical models of erosion in collisional orogens. Along a Trans-Himalayan transect in central Nepal, we develop a kinematic and thermal model to predict variations in bedrock cooling ages in modern Himalayan topography. The model assumes a thermal steady state and utilizes a simple ramp-and-flat-style decollement, representing the Main Himalayan Thrust. The model also assumes a topographic steady state, such that overthrusting is balanced by erosion to maintain a constant topographic profile. Erosion rates display strong spatial variations as a function of the angle between the slope of the topographic surface and the trajectories of rock particles approaching the surface. To predict the detrital cooling-age signal, we combine the distribution of bedrock cooling ages within a catchment with the rate of erosion and distribution of muscovite. Predicted cooling-age distributions are compared with detrital  $^{40}\text{Ar}/^{39}\text{Ar}$  muscovite data to assess varying tectonic and erosion scenarios. Such cooling-age distributions are very sensitive to how much of the total plate convergence is expressed as erosion of the overthrusting plate. The best fit model assigns 4–6 km Myr<sup>-1</sup> of overthrusting (equivalent to as much as 1.5–2 km Myr<sup>-1</sup> of vertical erosion) to the Asian plate. Although a trade-off exists between ramp geometry along the decollement and the best fit rate, only a narrow range of ramp dips, decollement depths, and erosionally compensated overthrusting rates are compatible with the observed detrital ages.

**Citation:** Brewer, I. D., and D. W. Burbank (2006), Thermal and kinematic modeling of bedrock and detrital cooling ages in the central Himalaya, *J. Geophys. Res.*, *111*, B09409, doi:10.1029/2004JB003304.

### 1. Introduction

[2] The complexities of the growth and erosion of orogenic belts underlie current debates on steady state orogens, tectonic impacts on climate change, and erosional controls on orogenic evolution. These debates commonly invoke the Himalaya, the icon of continental collision, because the temporal evolution of this orogen has been proposed as a prominent Cenozoic driving mechanism for strontium and carbon geochemical cycles [Derry and France-Lanord, 1996; Raymo *et al.*, 1988], climate change [Kutzbach *et al.*, 1993; Ruddiman and Kutzbach, 1989], and enhanced Late Cenozoic erosion [Zhang *et al.*, 2001]. Recent numerical models have greatly increased our insight into how orogenic systems may operate [e.g., Beaumont *et al.*, 1992, 2001, 2004; Koons, 1989, 1995; Willett, 1999], and despite the inevitable simplifications of numerical models, their results can provide new ideas and hypotheses to be evaluated with field data.

[3] Such data frequently include bedrock cooling ages that are used as a proxy for the erosion rate in order to infer spatial variations in deformation rates (e.g., Spotila *et al.* [1998], Fitzgerald *et al.* [1995], or Ruhl and Hodges [2005]). The amount of information one can extract from such analyses, however, is commonly limited by assumptions, including (1) vertical particle trajectories toward the surface, (2) horizontal isotherms, and (3) an estimated linear geothermal gradient. Given the intricacies of orogenic belts, these assumptions are frequently invalid. In collisional orogens, lateral advection of rock is usually faster than vertical advection and therefore dominates particle pathways through the orogen. This lateral rock movement, in combination with the effects of erosion and topography, will deflect isotherms and produce local, nonlinear, geothermal gradients [e.g., Batt and Braun, 1999; Beaumont *et al.*, 1992, 2001, 2004; Willett *et al.*, 2003]. Thus, to extract the maximum amount of geological information from detrital cooling ages, some of the complexities of regional tectonics need to be incorporated into numerical simulations. Only then can we understand how variations in deformation pathways, tectonic rates, topography, heat production, erosion rates, and lithology influence the spatial distribution of bedrock cooling ages.

[4] Increasingly complex numerical models, however, need to be tested against more comprehensive sets of field data. Thus we focus here on using modern detrital cooling-

<sup>1</sup>Department of Geosciences, Pennsylvania State University, University Park, Pennsylvania, USA.

<sup>2</sup>Department of Earth Science, University of California, Santa Barbara, California, USA.

age signals to constrain models of erosion in mountain belts. A detrital sample may be more advantageous than traditional bedrock thermochronology, because it is easily collected and provides an integration of cooling ages from an entire drainage basin, irrespective of glacial coverage or accessibility. In contrast, bedrock cooling ages are restricted to single locations, typically valley floors, and commonly comprise a limited number of samples that are difficult and expensive to collect.

[5] Investigations of individual basins [Brewer *et al.*, 2003; Stock and Montgomery, 1996; Ruhl and Hodges, 2005] and drainage networks [Brewer *et al.*, 2006] provide evidence that, given some simple assumptions, the detrital cooling-age signal can be systematically predicted, and detrital ages from the foreland can yield information about the tectonics of the hinterland [Bernet *et al.*, 2001; Carrapa *et al.*, 2003]. Yet, few such models account for the increasingly recognized effect of lateral advection of rock mass through an orogen. Geodynamic models [e.g., Beaumont *et al.*, 1992, 2001; Koons, 1989, 1995; Willett, 1999; Willett *et al.*, 2001] have addressed lateral advection, and several predict how the spatial distribution of bedrock cooling ages may change across an orogen [Willett and Brandon, 2002; Batt and Brandon, 2002; Jamieson *et al.*, 2004]. Although recent thermal and metamorphic investigations have also more commonly included lateral advection [Bollinger *et al.*, 2004; Harrison *et al.*, 1998; Henry *et al.*, 1997; Jamieson *et al.*, 1998, 2004], few combine advection with topography to predict the variability of cooling ages as a function of both topographic relief and kinematic pathways [Ehlers and Farley, 2003].

[6] Here, we present a methodology that allows us to combine geodynamic models with a digital elevation model (DEM) to predict detrital cooling ages in the central Nepalese Himalaya. Building on previous investigations, this methodology predicts both the spatial distribution of cooling ages within a landscape and the resulting detrital signal derived from eroding that bedrock. Whereas our thermal model does not have the sophistication of ramp timing, metamorphism, or melt generation that have been incorporated into some previous models [Harrison *et al.*, 1998; Henry *et al.*, 1997; Jamieson *et al.*, 2004], we have added the complexities of local topographic relief and catchment geometry in order to predict the detrital cooling-age signal.

[7] When combined with an assumed steady state topography, a basic two-dimensional (2-D) kinematic and thermal geodynamic model predicts (1) the position of the closure isotherm, (2) the distance a rock has to travel along a pathway to the surface, and (3) the rate of movement along that path. In conjunction with digital topography, this 2-D transect is extrapolated along strike into a 3-D model of bedrock cooling ages. The resulting map of bedrock cooling ages can be manipulated with GIS software to correct for variations in erosion rate and lithology in order to predict the detrital cooling-age signal from a catchment within the orogen. Comparison with the modern detrital cooling-age results allows us to place limits on 2-D kinematic-and-thermal models that are compatible with observed data, thereby providing insights into rates of Himalayan deformation.

[8] Although our area of investigation is the Marsyandi catchment in Nepal, the technique of predicting detrital

cooling-age signals from geodynamic models may be applied to other orogens and tectonic settings. With this methodology, detrital cooling-age signals derived from orogen-scale drainage basins can be used to evaluate competing tectonic and erosion hypotheses. To help calibrate models of mountain belt evolution through time, samples from foreland stratigraphic successions [Bernet *et al.*, 2001; Carrapa *et al.*, 2003] can be compared with model predictions of changing age distributions in hinterland source areas as a function of the kinematics of deformation and associated erosion.

## 2. Geological Background

[9] The Himalaya mark the southern boundary of a widespread expression of continental collision throughout central Asia. Since collision of India with Asia at  $55 \pm 5$  Ma [Searle, 1996], some  $\sim 2500$  km of subsequent continental convergence has been accommodated by thickening and uplift of the Tibetan Plateau [e.g., Dewey *et al.*, 1988; England and McKenzie, 1982], underthrusting of India [e.g., Powell and Conaghan, 1973; Nelson *et al.*, 1996], intracontinental orogeny [e.g., Molnar and Tapponnier, 1975], and strike-slip tectonics [e.g., Tapponnier *et al.*, 1986, 1982, 2001; Yin and Harrison, 2000]. The geodetic convergence rate between India and Asia is  $\sim 40$  km Myr<sup>-1</sup> [Bilham *et al.*, 1997; Wang *et al.*, 2001], a rate consistent with recent revisions [Paul *et al.*, 2001] of the NUVEL-1A estimates of Late Cenozoic convergence rates [DeMets *et al.*, 1994]. Although along-strike rate variations exist [Chen *et al.*, 2004],  $\sim 40$ –50% of the modern Indo-Asian convergence is currently absorbed across the main Himalayan chain. Spirit leveling investigations [Jackson *et al.*, 1992; Jackson and Bilham, 1994] predict that present-day convergence results in vertical rock uplift rates of up to 7 mm yr<sup>-1</sup> over the topographic divide of the Greater Himalaya [Bilham *et al.*, 1997].

[10] Our study area is located in central Nepal, where the Marsyandi River drains the southern edge of the Tibetan Plateau before flowing south through the main Himalayan chain (Figure 1) and debouching into the Ganges foreland basin. The Tibetan Zone in the north is characterized by a sequence of lower Paleozoic to lower Tertiary marine sedimentary rocks [Gansser, 1964; Le Fort, 1975; Ratschbacher *et al.*, 1994]. Tibetan zone strata are bound in the south by the South Tibetan Detachment (STD) system, a suite of down-to-the-north normal faults that includes the newly described Machapuchare-Phu Detachment [Searle and Godin, 2003], as well as the previously mapped Chame Detachment [Coleman, 1996]. In the study area, brittle faulting on the STD occurred after 18–19 Ma [Searle and Godin, 2003]. The southernmost part of the Tibetan Zone strata typically cap the highest Himalayan peaks, although in the study area, many high peaks lie south of the STD.

[11] Situated beneath the STD, the Greater Himalaya sequence comprises kyanite-to-sillimanite grade metasedimentary and metaigneous rocks of Neo-Proterozoic to Cambrian-Ordovician age [Amidon *et al.*, 2005a; DeCelles *et al.*, 2000; Ferra *et al.*, 1983; Gehrels *et al.*, 2003; Parrish and Hodges, 1996]. Anatectic melting within the Greater Himalaya, commonly of the lower kyanite-grade schists of formation I [Barbey *et al.*, 1996; Harris and Massey, 1994],

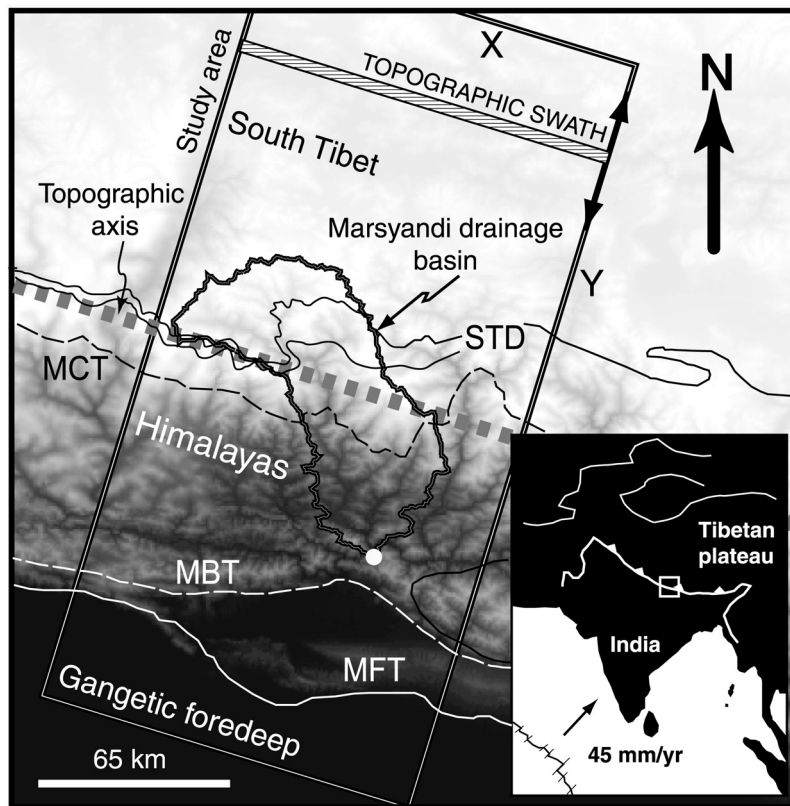


**Figure 1.** Location of the Marsyandi drainage basin and the study area, aligned with the strike of the orogen. The white dot indicates the location of the detrital thermochronological sample at the mouth of the Marsyandi catchment (S-24 [Brewer *et al.*, 2006]). The topography is derived from a 90-m DEM and GTOPO30 where 90-m data are missing. The approximate location of the topographic axis and the major faults are shown for reference. The hatched area shows a representation of the strike-parallel swath that is scrolled normal to the strike to define mean topographic characteristics (see Figure 3). Inset shows general location of study area. MBT, Main Boundary Thrust; MFT, Main Frontal Thrust; MCT, Main Central Thrust; STD, South Tibetan Detachment.

produces leucogranites that intrude the top of the sequence. In the study area, the crystallization of the Manaslu leucogranite has been dated at  $22.4 \pm 0.5$  Ma using  $^{232}\text{Th}/^{208}\text{Pb}$  in monazite [Harrison *et al.*, 1995] and contains an older inherited-Pb monazite population of  $\sim 600$  Ma [Copeland *et al.*, 1988]. The Manaslu granite typically yields  $^{40}\text{Ar}/^{39}\text{Ar}$  muscovite plateau dates of  $\sim 17$  to 18 Ma [Coleman and Hodges, 1995; Copeland *et al.*, 1990].

[12] The south vergent Main Central Thrust (MCT) is traditionally defined as the base of the kyanite-grade Greater Himalaya sequence where it overthrusts the Lesser Himalayan sequence [Colchen *et al.*, 1986]. This structural boundary is characterized by abrupt changes in  $\epsilon_{\text{Nd}}$  and in populations of U/Pb zircon ages [Martin *et al.*, 2005]. Early motions on the MCT were synchronous with the regional metamorphism of the Greater Himalaya sequence at 20 to 23 Ma [Hodges *et al.*, 1996]. Major motion of the MCT is typically interpreted to have stopped in the Middle Miocene. Recently, several studies have inferred significant Pliocene or younger reactivation of the MCT, or younger thrusts in its proximal footwall, on the basis of ages of synkinematic monazites [Catlos *et al.*, 2001; Harrison *et al.*, 1997], late Miocene and younger  $^{40}\text{Ar}/^{39}\text{Ar}$  bedrock and detrital cooling ages [Edwards, 1995; Macfarlane *et al.*,

1992; Wobus *et al.*, 2003], steep topographic gradients [Wobus *et al.*, 2003, 2005], brittle faulting of ductile fabrics [Hodges *et al.*, 2004], and the southern limit of significant Himalayan metamorphism [Searle and Godin, 2003].

[13] The Lesser Himalayan sequence predominantly comprises greenschist grade metasediments [Colchen *et al.*, 1986] that are Mesoproterozoic to Early Cambrian in age [see Hodges [2000] for review]. The southern limit is bound by the south vergent Main Boundary Thrust, interpreted to have initiated between 9 and 11 Ma [Meigs *et al.*, 1995]. Its most recent movement is difficult to constrain, but must be younger than early Pliocene in Nepal [DeCelles *et al.*, 1998]. The Main Frontal Thrust (MFT) represents the distal expression of Himalayan deformation in the foreland. In central Nepal, the MFT displays a well-documented shortening rate of  $\sim 20$  km  $\text{Myr}^{-1}$  over the Holocene [Lavé and Avouac, 2000], indicating that it is currently the major active fault in the study area. Although this rate suggests that all of the Himalayan geodetic convergence is accommodated on this southernmost structure, lower rates on the analogous structure in India [Wesnousky *et al.*, 1999] imply that the fraction of the total shortening accommodated by the MFT varies along strike. Similarly, abrupt discontinuities in cooling ages and erosion rates suggest the presence

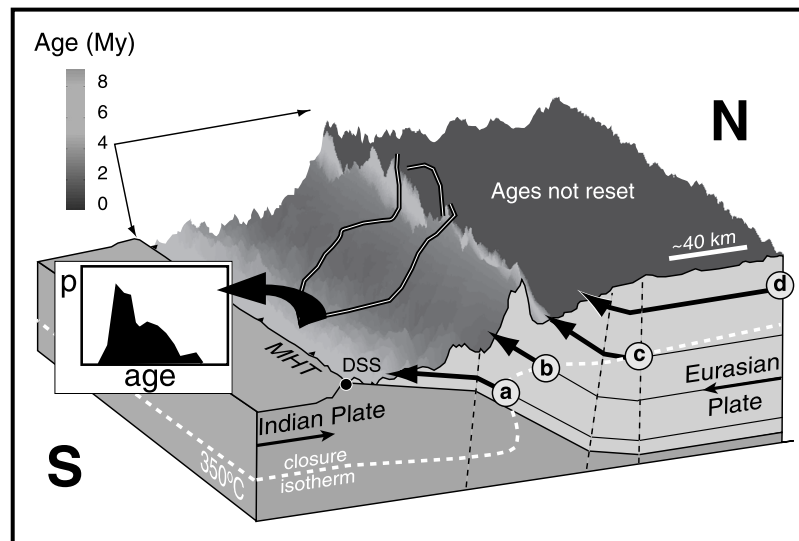


**Figure 2.** Conceptual basis for the combined thermal, kinematic, and detrital model. With a simplified ramp flat geometry and known overthrusting rate, the velocity (speed and trajectory angle) of particles through the orogen can be calculated. Within the predetermined kinematic framework, the thermal structure after 20 Myr is calculated, and the depth of the closure temperature (white dashed line) for muscovite ( $350^{\circ}\text{C}$ ) is extracted. The 2-D thermal structure is extrapolated along strike into three dimensions, and a 90-m DEM is used to calculate how long it takes each point in the landscape to pass from the depth of the closure isotherm to the surface along the specified particle path (distance of the black arrows divided by the overthrusting rate of Eurasia with respect to the decollement/surface singularity (DSS) which is used as a reference marker). The youngest ages are created by trajectory b because the  $350^{\circ}\text{C}$  isotherm is closest to the surface along this trajectory. Trajectory a produces the oldest cooling ages because it travels along a flat (under the Lesser Himalaya) before reaching the surface. Particles moving along trajectory c travel the further than trajectory b and give intermediate ages, whereas trajectory d advects rock into the orogen above the closure temperature and so can be assigned an original rock age. The insert depicts a hypothetical probability (P) distribution of detrital ages from the outlined catchment.

of Quaternary faults within the Lesser Himalaya [Wobus *et al.*, 2003, 2005].

### 3. Thermal and Kinematic Modeling

[14] As opposed to simple vertical motion of rocks, lateral advection during continental collision often represents the dominant component of the deformation field [Willett, 1999]. Yet, within the geochronological community, cooling ages have typically been interpreted considering only one dimension, with erosion rates calculated assuming that the rock column is moving vertically toward the surface [e.g., Fitzgerald *et al.*, 1995]. In contrast to most such studies, Harrison *et al.* [1998] and Jamieson *et al.* [2002, 2004] used 2-D kinematic-and-thermal modeling to investigate anatexis and metamorphism in the Himalaya. Their models should provide a better comparison to thermochronological data because bedrock ages are predicted by tracing particle trajectories through the orogen.

[15] We adopt a similar approach and present a 2-D kinematic-and-thermal model to determine the depth of the closure temperature and calculate the path of rock particles through an orogenic transect. To do this, we define a decollement geometry within the Himalaya (section 3.1) and specify the thermal characteristics of the orogen (section 3.2). We subsequently extrapolate the 2-D solution

along strike to predict the 3-D spatial distribution of bedrock cooling ages over the entire landscape (Figure 2). Correcting for spatial variations in the abundance of the target mineral for dating (section 3.3), GIS software allows us to use the resulting “age maps” to extract a modeled detrital cooling-age signal. We then compare signals predicted from different scenarios to observed detrital cooling ages [Brewer *et al.*, 2006] to assess which model parameters are consistent with the data and to test the model’s sensitivity to variations in these parameters.

#### 3.1. Constraints on Thrust Geometry

[16] In an active orogen, a bedrock cooling age represents the time elapsed since a rock particle passed through the closure temperature and subsequently reached the surface. Therefore, in order to predict a bedrock cooling age, we need to know (1) the position of the closure isotherm with respect to the surface, (2) the particle trajectory toward the surface, and (3) the rate of particle transport along this trajectory. Because of the strong dependence of the thermal structure on the rate of rock advection toward the surface [Batt and Brandon, 2002; Mancktelow and Grasemann, 1997; Stüwe *et al.*, 1994], the kinematic structure of the mountain belt is a primary parameter to constrain. By combining heat production with the velocity (speed and direction) of particles through the orogen, we model thermal

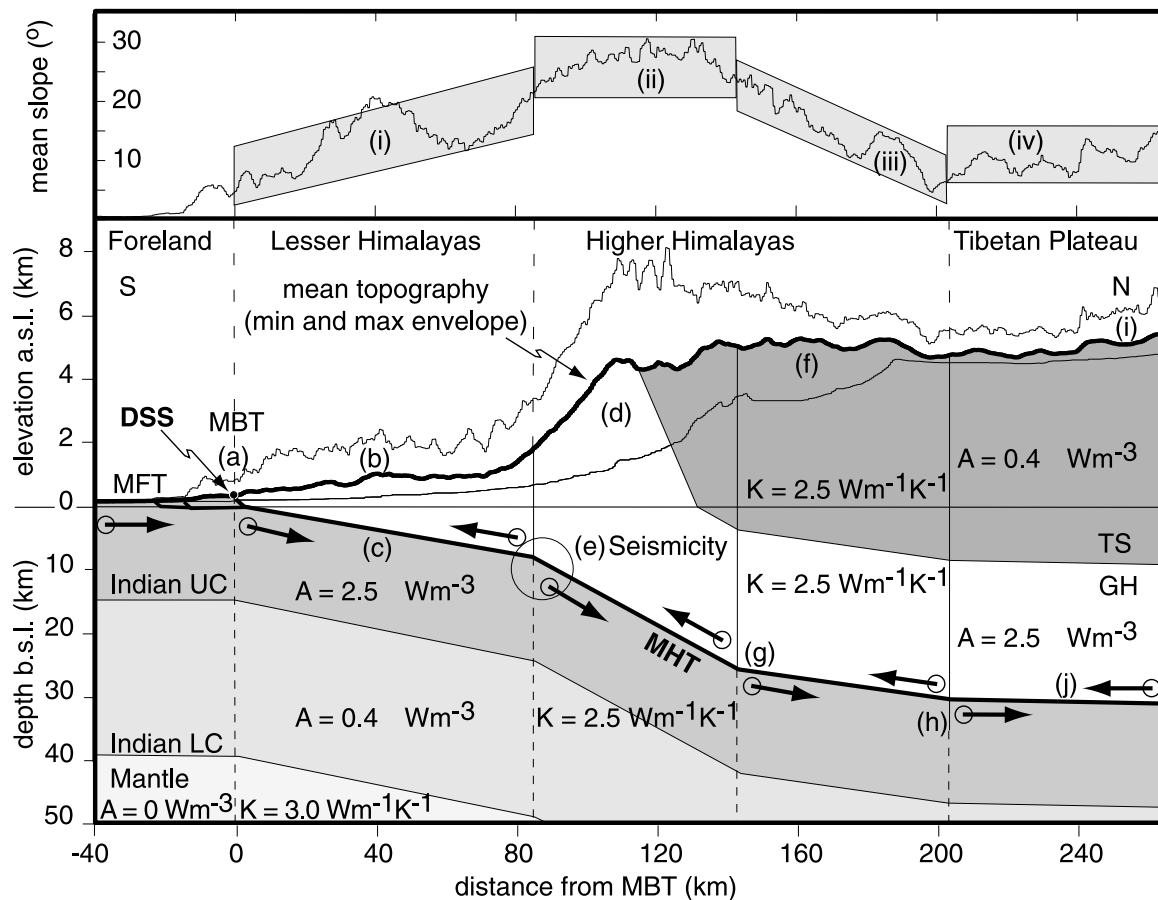


**Figure 3.** Constraints used for the kinematic-and-thermal model. (top) Mean slope calculated over a scrolling swath (Figure 1) divided into four domains (i–iv). (bottom) Thermal conductivity ( $K$ ) and radioactive heat production ( $A$ ) assigned to the Tibetan zone sediments (TS), Greater Himalayan sequence (GH), and the Indian upper crust (UC) and lower crust (LC). The Main Himalayan Thrust (MHT) ramp geometry that we initially use is illustrated, cropping out at the location of the Main Boundary Thrust (MBT). The approximate location of the Main Frontal Thrust (MFT) is indicated. Note the change in scale above sea level to illustrate the minimum, maximum, and average elevations. Constraints on ramp position are discussed in the text (section 3.1).

conditions and, more specifically, the position of the closure isotherm.

[17] We invoke several simplifications and assumptions to define the kinematic structure. First, we use a 2-D model. Because of sparse subsurface structural data, it is necessary to extrapolate geometrical constraints along strike to calibrate our modeled transect. Given the remarkable lateral continuity in the overall structure of the Himalayan orogen [Hodges, 2000], a 2-D approximation is probably reasonable for the along-strike scale of 100 to 200 km in our model. Second, despite the complex structural architecture of the Himalaya, we use a single decollement to model the kinematics. A major plate-scale decollement, the Main Himalayan Thrust, has been proposed to underlie the Himalaya, with surface faults soling out into this decollement [Bollinger *et al.*, 2004; Schelling, 1992; Seeber *et al.*, 1981]. Third, we specify a decollement comprising planar segments that meet at kink bends [Suppe, 1983]. Whereas few data exist to assess whether, at the scale of the Himalayan orogenic belt, fault surfaces are approximately planar and fault dips change abruptly (as assumed with kink

bends), these assumptions do allow simple tracking of particle paths.

[18] Because our focus is on the major kinematic characteristics of the orogen, rather than local complexities, we adopt this simple orogenic-scale decollement model. A similar approach was taken by Henry *et al.* [1997], who modeled the 2-D thermal structure of the Himalaya using a single crustal-scale decollement dipping at  $10^\circ$  northward from the surface outcrop of the Main Boundary Thrust. We use a more complex decollement that has 4 dip domains (Figures 2 and 3), with kink band folding in the overlying thrust sheet, to mimic the assumed large-scale structure of the orogen [Lavé and Avouac, 2001; Bollinger *et al.*, 2004]. In our analysis, the Main Himalayan Thrust is defined as the main active boundary between the Indian and Asian plates, even though rocks derived from the Indian plate have been accreted to the Asian plate and now lie above the basal detachment to form the modern Himalaya.

[19] With our simplified structure, the Main Boundary Thrust (MBT) represents the surface expression of the Main Himalayan Thrust (Figure 3, point a). It is recognized,

however, that the Main Frontal Thrust actually represents the southernmost active structure in this region [Lavé and Avouac, 2000; Lavé et al., 2005]. Our model ignores this region to the south of the MBT, however, because the gentle-to-horizontal dip and the shallow depth of the decollement [Schelling, 1992] dictate that movement is insufficient to have exhumed reset muscovite ages and that only foreland-basin strata are being deformed. The average position of the MBT in the study area is constrained by the geomorphic expression of the southern edge of the Lesser Himalaya, taken from the 90-m DEM. In our model, the Main Himalayan Thrust dips at  $5^\circ$  to  $6^\circ$  north beneath the Lesser Himalaya (Figure 3, fault segment c), consistent with inferences from geological sections [Schelling, 1992], borehole data [Mathur and Kohli, 1964], and leveling data [Jackson et al., 1992].

[20] From the shallow Lesser Himalayan decollement, we model an  $18 \pm 5^\circ$  midcrustal ramp dipping beneath the Greater Himalaya (Figure 3) because several lines of evidence suggest that the Main Himalayan Thrust steepens beneath the main topographic escarpment of the Himalaya. Foliation planes in the northern Lesser Himalaya steepen northward [Schelling and Arita, 1991] and are interpreted to represent a transition from a flat decollement to a ramp under the topographic front. Receiver functions indicate a steeper dip to the Moho beneath the Himalaya to the north of the Lesser to Greater Himalaya transition [Nábelek et al., 2005]. A cluster of seismicity, ranging from 5 to 20 km depth and centered approximately 80 km north of the Main Frontal Thrust (Figure 3, area e) [e.g., Ni and Barazangi, 1984], has been interpreted to result from stress release on this steeper section of the Main Himalayan Fault [Pandey et al., 1995]. Spirit leveling indicates short-term rock uplift rates of 4 to 7 mm yr<sup>-1</sup> occur over 40-km wavelengths in the Higher Himalaya, and 2-D dislocation modeling indicates that this can result from strain accumulation above a steeper section on a deep decollement [Jackson et al., 1992; Bilham et al., 1997]. In addition, gravity investigations suggest that the Moho dips at  $15\text{--}20^\circ$  under the topographic front of the Himalayas, implying a sharp bend in the Indian plate [Lyon-Caen and Molnar, 1983].

[21] The modeled position of the Main Himalayan Thrust to the north of the midcrustal ramp is consistent with INDEPTH seismic imaging of a major northward dipping reflector under southern Tibet, interpreted to be the interface between the Indian and Eurasian plates [Brown et al., 1996; Nelson et al., 1996]. Beneath the South Tibetan Detachment system, this ramp is at a two-way traveltime of 9 s ( $\sim 30$  km depth) (Figure 3, point g). The ramp extends  $\sim 65$  km northward to where it disappears at a depth of  $\sim 35$  km under the southern edge of the Kangmar Dome [Nelson et al., 1996].

[22] Existing geologic data in the study area do not precisely define the position of specific bends in the decollement. We therefore use the topography as a guide to changes in the underlying ramp geometry. We use a swath  $\sim 130$  km long by 0.6 km wide, oriented with the long axis parallel to the strike of the orogen (Figure 1), to extract averaged topographic characteristics of the study area from a smoothed 90-m DEM, and from a map of hillslope angles with values calculated using a 180 m by 180 m area. On the basis of slope angles (Figure 3, top) and elevation character-

istics (Figure 3, bottom), we divide the study area into four regions. In the north, low hillslope angles (Figure 3, slope domain iv) and low relief (Figure 3, area i) predominate on the edge of the Tibetan Plateau. Despite the high elevations of the Tibetan Plateau, we interpret this low-relief region to be characterized by low erosion rates. In our model, rock is advected laterally, and we specify a nearly horizontal decollement (Figure 3, fault segment j) to represent this northernmost section beneath southern Tibet. To the south, a zone of increasing relief (Figure 3, area f) and steepening slopes (Figure 3, slope domain iii) corresponds to the headwaters of Himalayan transverse rivers. We interpret these changes to be a response to rock uplift above a gently inclined ramp in the MHT (Figure 3, points g and h). The maximum elevation envelope descends to the north across this zone at  $\sim 2^\circ$  (Figure 3), which, in the absence of erosion, could indicate the dip of the ramp. Because Tethyan strata are preserved across this zone, the magnitude of Cenozoic erosion must remain less than a few kilometers. Given this, if we restore an estimated eroded thickness of 2 to 3 km [Searle and Godin, 2003] to the southern end of this zone where relief is greatest, the ramp angle is estimated to be  $\sim 4^\circ$ : the dip we utilize.

[23] Still farther south, the Main Himalayan Thrust is interpreted to attain its steepest dip beneath the Greater Himalaya. As material is transported over the ramp inflection point (Figure 3, point g), relief markedly increases (Figure 3, area d), slopes are steep (Figure 3, slope domain ii), and Tethyan strata are rapidly stripped off. We interpret the high relief (up to 6 km) and steep slopes to indicate both hillslopes at the threshold angle for landslide failure [Burbank et al., 1996] and high erosion rates due to the increased rate of vertical advection above the steep ramp. Apatite fission track ages are young ( $< 1$  Myr) across the Greater Himalaya, suggesting both rapid and spatially uniform Quaternary erosion [Burbank et al., 2003]. The minimum elevations show a rapid increase northward suggesting that the rivers increase in gradient in response to an increased rock uplift rate [Duvall et al., 2004; Seeber and Gornitz, 1983; Whipple and Tucker, 1999] above the inferred Main Himalayan Thrust ramp (Figure 3, area d). If a topographic steady state is assumed in the Himalaya, the steeper and narrower rivers suggest that the most rapid fluvial erosion and rock uplift occur across this zone [Lavé and Avouac, 2001]. The lower relief (Figure 3, region b) and lower hillslopes (Figure 3, slope domain i) of the Lesser Himalaya are interpreted to be underlain by a gentler ( $\sim 5^\circ$ ) ramp of the Main Himalayan Thrust (Figure 3, fault segment c). We interpret that this change to lower relief represents a new balance between erosion processes and rock uplift. Because of the decrease in vertical rock uplift rates as lateral advection becomes more dominant, less potential energy per unit time is added to the landscape.

### 3.2. Thermal Model

[24] To determine the cooling age of a specified thermochronometer, a thermal model is needed to predict the depth of the closure isotherm. Because the results of the model are compared against the  $^{40}\text{Ar}/^{39}\text{Ar}$  analyses of muscovite from Brewer et al. [2006], we employ a nominal closure temperature of  $350^\circ\text{C}$  [McDougall and Harrison, 1999]. Our thermal model has three main components: (1) the kinemat-

ics which are controlled by the decollement geometry (as discussed) coupled with rates of overthrusting and erosion, (2) the geometry and thermal properties assigned to each thermo-lithological unit (radioactive heat production, conductivity, and diffusivity), and (3) a shear heating term that represents frictional heating on the main decollement. The parameterization of our thermal model (Figure 3) closely resembles that of *Henry et al.* [1997], with a thermally inhomogeneous crust underlain by mantle characterized by negligible heat production and a conductivity of  $3.0 \text{ W (m } ^\circ\text{K)}^{-1}$  [Schatz and Simmons, 1972]. The Indian crust is assumed to be bilayered with a 15-km-thick upper crust with heat production of  $2.5 \mu\text{W m}^{-3}$  [England et al., 1992], and a 25-km-thick lower crust with heat production of  $0.4 \mu\text{W m}^{-3}$  [Pinet, 1992]. With our kinematic model, the Lesser Himalaya and the Greater Himalaya sequence function as a single tectonic unit and are assigned a heat production of  $2.5 \mu\text{W m}^{-3}$  due to high concentrations of radioactive elements [England et al., 1992].

[25] The thickness of the Greater Himalaya sequence varies laterally within the Marsyandi study area, perhaps due to South Tibetan Detachment system normal faulting at the top of the slab (which is not included in this model). Nevertheless, we specify a constant thickness of 22 km for the Greater Himalaya sequence that is consistent with the INDEPTH geological section, measured from the Main Himalayan Thrust to the South Tibetan Detachment system [Nelson et al., 1996]. As a consequence, Tethyan rocks crop out on the highest peaks in our model, matching the typical geology of the range [Colchen et al., 1986]. Because of the normal faulting and lateral thickness variations, however, the thickness of 22 km is simply a thermal parameter for the model, rather than an accurate predictor of the surface outcrop of Tethyan strata. Because they contain a lower abundance of radioactive isotopes, the Tethyan strata are assigned heat production of  $0.4 \mu\text{W m}^{-3}$ . Crustal conductivity and thermal diffusivity are set uniformly to  $2.5 \text{ W (m } ^\circ\text{K)}^{-1}$  and  $0.8 \text{ mm}^2 \text{ s}^{-1}$ , respectively. The surface boundary condition is set to  $0^\circ\text{C}$ , with the morphology of the interface determined by the mean elevation (Figure 3).

[26] Because of our 2-D approach, the cooling effects of relief variations along strike are ignored, and when extrapolating the thermal model laterally, we assume no significant deflection of the  $350^\circ\text{C}$  isotherm by local topography [Brewer et al., 2006]. The basal boundary is set to a constant mantle heat flow of  $15 \mu\text{W m}^{-2}$  that is consistent with values from Precambrian cratons [Gupta, 1993]. A constant geothermal gradient is applied to lateral boundaries experiencing an influx of rock mass into model space, while zero heat flow boundaries are specified if there is a net loss of mass from the system. A shear heating term, described by *Henry et al.* [1997], is used to account for frictional heating along the basal decollement fault. Heat production is a function of the shear stress and strain rate in both the brittle and the ductile regime. Shear stress is calculated as the minimum of a brittle lithostatic pressure-dependent law (1/10th the lithostatic pressure) or a ductile temperature-dependent power law, with parameters taken from the moderate friction flow law of *Hansen and Carter* [1982]. In the ductile regime, the fault zone is 1000 m wide and undergoes uniform strain and heating. This model predicts

that the brittle-to-ductile transition occurs at  $\sim 420^\circ\text{C}$  in the undeformed Indian Plate (see discussion by *Henry et al.* [1997]).

[27] The initial condition of the model is set by calculating a geothermal gradient [Pollack, 1965] for the thermal structure undergoing no heat advection. A 2-D finite difference algorithm [Fletcher, 1991] is used to define the thermal structure after  $\sim 20$  Myr of advection of rock mass through the orogen. This approximates a steady state solution, given the thermal response times of the  $350^\circ\text{C}$  isotherm: from initial static conditions, for a crustal column undergoing vertical erosion from depths of 35 km at rates of  $0.1$  to  $3.0 \text{ km Myr}^{-1}$ , 90 to 95% of the steady state solution is obtained in  $<10$  Myr [Brewer et al., 2003]. The morphology of the surface boundary in our model is not time-dependent, i.e., the topography is in steady state and, as a consequence, spatial fluctuations in the mean elevation across the orogen are invariant over timescales  $>1$  Myr and spatial scales of  $>100$  km. This implies that the rock influx into the orogenic front by overthrusting is necessarily balanced by denudation over these timescales.

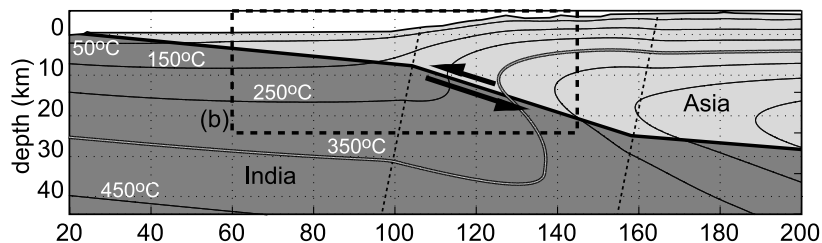
### 3.3. Particle Trajectories and Detrital Cooling-Age Signals

[28] Given the specified geometric architecture, plate convergence rate, and erosion rate, the thermal steady state (Figure 4a) in the overthrusting plate is a balance between three competing processes. The underthrusting plate comprises relatively cold material and so cools the overthrusting plate from beneath, resulting in a downward deflection of the closure isotherm. In contrast, hotter material from depth is overthrust into the orogen where erosion removes the cooler near-surface rocks, thus heating the overall system and moving the closure isotherm toward the surface. Counteracting this, from the top of the overthrusting plate, conductive heat loss to the atmosphere cools the orogenic surface.

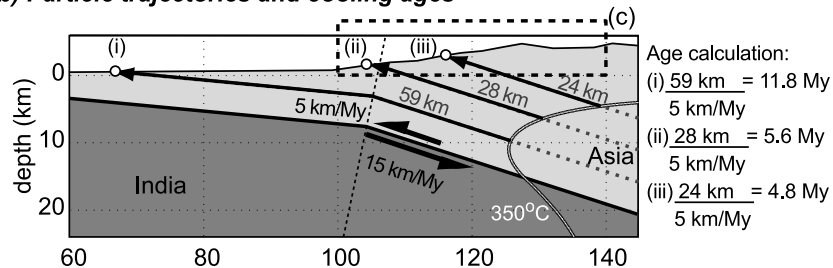
[29] Once the steady state thermal structure has been defined, we use the kinematic framework, with topography assumed to be in steady state, to predict cooling ages in the overthrusting plate. On the basis of fault bend fold theory [Suppe, 1983], the velocity vector for each point within the transect is calculated from the geometry of the underlying ramp, such that particle trajectories can be traced through the orogen. The distance traveled by a particle between passing through the argon closure temperature for muscovite ( $\sim 350^\circ\text{C}$ ) and reaching the surface (Figure 4b) can be converted into a cooling age by dividing by the velocity.

[30] Given that cooling age is a function of distance traveled since passing through the closure temperature, topographic relief will cause ages to vary at kilometeric scales, because the relief on the  $350^\circ\text{C}$  isothermal surface at depth is considerably dampened in comparison to surface relief (Figure 4c). To investigate this topographic effect on cooling ages, we assume that the geometry of the Main Himalayan Thrust is invariant across the width of the study area. This allows us to extrapolate the two-dimensional thermal model laterally to predict a quasi-3-D thermal structure and then use it in conjunction with digital topography to predict cooling ages as a function of landscape position. For any particular location, we measure the distance traveled along the trajectory from the modeled closure

## a) Thermal model



## b) Particle trajectories and cooling ages



## c) Topographic influence

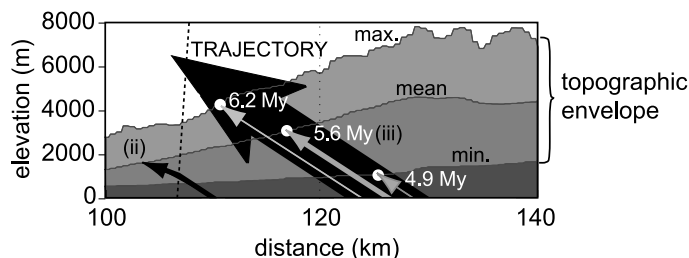


**Figure 4.** Three components needed to construct cooling ages for the landscape. (a) Depth of the 350°C isotherm modeled for the specified overthrusting rate and ramp geometry. In this example, the total convergence rate was partitioned into 15 km Myr<sup>-1</sup> of Indian underthrusting and 5 km Myr<sup>-1</sup> of erosionally compensated Asian overthrusting. (b) An enlarged portion of Figure 4a illustrating how the cooling ages are calculated. The distance a particle travels between passing through the closure temperature and reaching the surface (indicated by the black arrows) is divided by the Asian overthrusting rate. (c) Particles following the same flow line in 2-D travel different distances along strike because a 3-D landscape has a range of topography. Hence, when the real topography is used, each incremental change in the transect location along strike results in a different pattern of predicted bedrock cooling ages. The ages of maximum, minimum, and mean topography are illustrated.

temperature isotherm to the actual elevation of that point, thereby, creating a “cooling-age map” for the modern landscape (Figure 2).

[31] The translation of this cooling-age map into a detrital cooling-age signal, however, requires further analysis and is not a simple function of the areal distribution of ages. The relative proportion of grains of a certain cooling age from a detrital sample depends upon both (1) the fraction of land with that cooling age and (2) how fast that fraction is eroding. The former is calculated with the kinematic and thermal model in combination with the DEM, but the latter is more problematic.

[32] In the presence of rapid lateral advection, both the 2-D velocity field and the aspect of the topography in relation to it have to be considered. For illustration, consider erosion on the edge of a plateau in topographic steady state (Figure 5). Deformation occurs as material advects

laterally toward the plateau margin, along an underlying decollement and onto a steeper ramp. With this scenario, the highest erosion rate occurs where the aspect of the topography is normal to the particle trajectory (Figure 5, condition i), whereas the lowest erosion rate occurs when the topography is parallel with the velocity field (Figure 5, condition iii). Hence erosion is low across Tibet, increases above the 4° ramp, and becomes most rapid where the underlying ramp dips steeply in one direction and the average surface topography dips in the opposite direction, as is the case south of the Himalayan crest. When the range front slopes steeply toward the foreland, the vertical erosion rate (Figure 5, vector ii) underestimates the rate of rock removal perpendicular to the transport vector (Figure 5, condition i).

[33] Given this relationship, the volume of rock eroded ( $V$ ) in time ( $dt$ ) for a DEM with cell dimensions  $X$  by  $Y$  is a

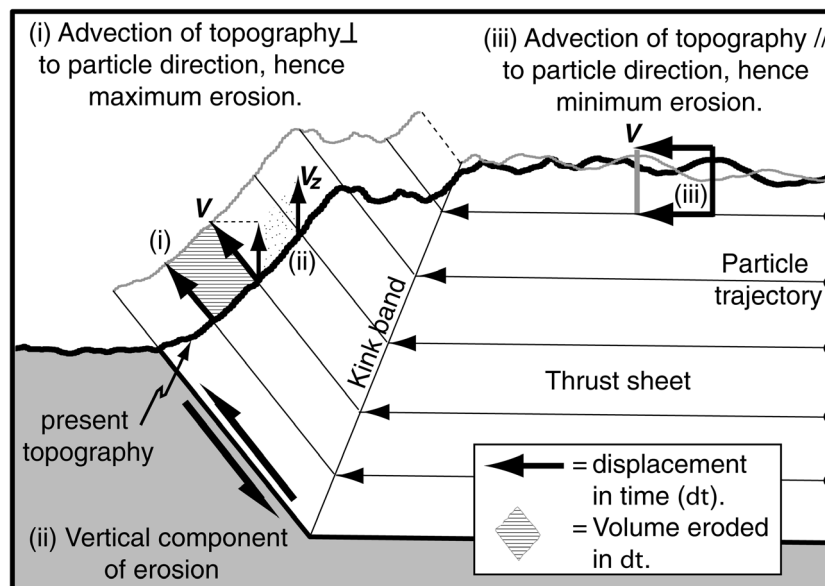


**Figure 5.** Volume of material eroded in a time increment ( $dt$ ) depends upon the aspect of the topography in relation to the particle velocity ( $V$ ). The black topography is the present topographic profile. The gray line mirroring the present topography illustrates the volume of rock eroded in  $dt$  with an assumption of complete steady state conditions. When the particle velocity is normal to the topography, maximum volumes of material are eroded (condition i). When the particle velocity is parallel to the topography, the topography becomes advected laterally and little erosion occurs (condition iii). Note that the volume of eroded material is underestimated if solely the vertical component ( $V_z$ ) of the particle velocity is used in the calculation (condition ii).

function of the topographic slope and particle velocity ( $v$ ) in the plane of  $Y$ :

$$V(dt) = \left( \frac{Y}{\cos \alpha} \right) v dt \sin(\beta) X \quad (1)$$

The values  $\beta$  and  $\alpha$  are dependent upon the relationship between the topographic surface slope ( $S$ ) and the underlying ramp angle, as defined in Figure 6. Using equation (1), the effects of topographic slope and particle trajectory on the volume of material eroded can be predicted for a grid cell of unit area, undergoing erosion for unit time (Figure 7). With vertical erosion (particle trajectory angle =  $90^\circ$ ), erosion is independent of the surface slope (unit erosion everywhere). The highest erosion rates, per unit horizontal area, for slopes of  $30$ – $40^\circ$  (as is typical in the Himalaya) occur with particle trajectories of  $50^\circ$  to  $60^\circ$ , and the lowest erosion rates occur as particle trajectories approach  $0^\circ$ .

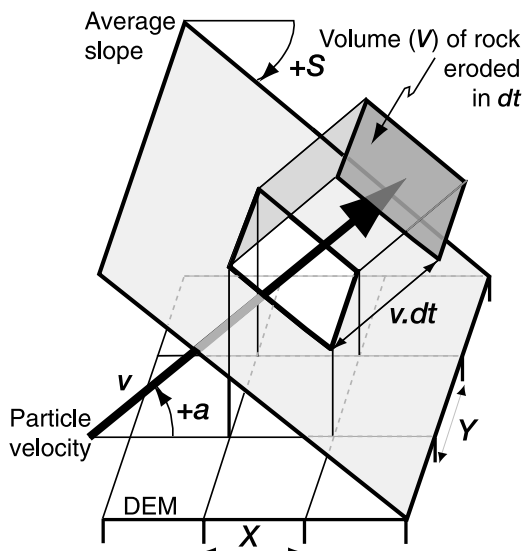
[34] An assumption of this methodology is that topographic steady state [Willett and Brandon, 2002] is maintained. For our purposes, this means that spatially averaged characteristics (hypsometry, slope distributions, along-strike averaged morphology) do not vary over the interval of interest, which is several millions of years in this study. Although the local topography is expected to vary at a point and the mean topography may vary at climatic timescales ( $10^3$ – $10^5$  years), this variability at orogenic timescales ( $>10^6$  years) is assumed negligible with respect to long-term, mean topographic characteristics. Hence, for the thermal modeling, we use the modern mean elevation as our topographic surface boundary.

[35] To minimize the effects of local and short-term deviations from the average topography, we divide the orogen into three zones (Figure 8) based upon the overall aspect (with respect to the plate velocity vector) of mean elevation: the Tibetan Plateau, the Himalayan front, and the Lesser Himalaya. These strike-parallel zones are used in combination with the underlying ramp geometry to calculate an “erosion rate map” in which rates vary as orogen-parallel swaths.

[36] To predict the distribution of detrital ages produced from the landscape, we integrate the volumetric contribution of modeled cooling ages from each pixel across the area. We present this as a probability density function (PDF), which represents the probability of a particular cooling age being found in the sediment and is equivalent to the theoretical PDF of Brewer *et al.* [2003]. Given homogeneous lithology, the theoretical PDF with probability of dating a grain of a particular age ( $P_a$ ) as a function of age ( $a$ ) can be calculated for a DEM matrix containing  $x$  by  $y$  cells:

$$P_a(a) = \sum_{X=0}^{X=x} \left[ \sum_{Y=0}^{Y=y} \left[ \tau(X, Y) \frac{dv}{dt}(X, Y) \right] \right] \quad (2)$$

where  $dv/dt$  is the volume of material a grid cell contributes per unit time. The value  $\tau$  has to be computed for each grid cell location ( $X, Y$ ) and for each value of  $P_a(a)$ : if the cooling age ( $a_c$ ) value of a cell is equal to  $a$ , then  $\tau = 1$ ; otherwise,  $\tau = 0$ . The area under the resulting curve is normalized to unity and in this study, we apply a 0.5 Myr smoothing function to the PDF to minimize the effects of small perturbations. This approach assumes a steady state



$$V(dt) = \left( \frac{Y}{\cos \alpha} \right) v dt \sin(\beta) X$$

condition	$\beta$	$\alpha$
$S + a < 90^\circ$	$S + a$	$S$
$S + a > 90^\circ$	$180^\circ - (S + a)$	$S$
$S > 90^\circ$ and $a > (180^\circ - S)$	$a - (180^\circ - S)$	$270^\circ - S$

**Figure 6.** Calculation of volume ( $V$ ) of rock eroded in time increment ( $dt$ ) for one digital elevation model (DEM) grid cell, assuming a steady state landscape. The volume of rock eroded for a given particle speed ( $v$ ) over time ( $dt$ ) is dependent upon the topographic slope ( $S$ ) and particle direction, which is controlled by the angle of the underlying thrust ramp ( $a$ ). If  $S + a < 90^\circ$ , then  $\beta = (S + a)$  and  $\alpha = s$ . If  $S + a > 90^\circ$ , then  $\beta = 180 - (S + a)$  and  $\alpha = s$ . If  $S > 90^\circ$ , then a volume can only be calculated if  $a > (180 - S)$  in which case  $\beta = a - (180 - S)$  and  $\alpha = 270 - S$ ; otherwise, the calculated volume becomes negative because the particle trajectory is directed into the slope, as opposed to out of it. Both angles,  $S$  and  $a$ , are measured positively, and the calculation assumes that the strike of the topography is perpendicular to the particle transport direction.

topography, no significant sediment storage within the drainage basin, and no mechanical comminution of muscovite within the fluvial system. Within mountain belts undergoing high erosion rates ( $>1 \text{ km Myr}^{-1}$ ), simple geometric calculations show that volumetrically significant sediment storage of sufficient duration ( $>0.5 \text{ Myr}$ ) to affect the detrital age is unlikely over the hinterland-to-foreland spatial scale. *Brewer et al.* [2006] argued that comminution of muscovite through the Marsyandi River system had an undetectable impact, given the uncertainty in the analysis of  $^{40}\text{Ar}/^{39}\text{Ar}$  ages. Moreover, the distribution of detrital zircon fission track ages from the same river [*Burbank et al.*, 2006] mimics that of the muscovite  $^{40}\text{Ar}/^{39}\text{Ar}$  ages, but is offset toward younger ages by 1–2 Myr: an offset commensurate with the lower closure temperature of zircon.

[37] With our model, the dependencies between the predicted cooling-age signal and geological parameters

can be investigated. Initially, we focus on the extent to which observed detrital cooling ages [*Brewer et al.*, 2006] place limits on the rate of overthrusting and erosion of “Asia” versus underthrusting of India, and we evaluate the sensitivity to different ramp geometries. Given the closure isotherm’s dependence on (1) cooling by the underthrusting plate, (2) heating due to lateral advection of hot material into the system, and (3) conductive heat loss to the atmosphere (Figure 4a), kinematic variations should be evident in the predicted distribution of bedrock, and therefore detrital, cooling ages.

[38] Subsequently, we examine the effects of drainage basin area and lithological factors by modeling the detrital signal from the modern Marsyandi River and comparing the results to observed data [*Brewer et al.*, 2006]. Because it is the best proxy for the distribution of cooling ages delivered to the foreland, we use the most downstream Marsyandi River sample (Figure 1) to integrate across the broadest area possible. *Brewer et al.* [2006] dated 55 muscovite grains from this sample at the  $^{40}\text{Ar}/^{39}\text{Ar}$  laser microprobe facility at the Massachusetts Institute of Technology.

[39] The  $^{40}\text{Ar}/^{39}\text{Ar}$  data (Figure 9) are presented as a summed probability density function (SPDF), comprising the normalized summation of individual grain PDFs; which in turn represent each grain age with a Gaussian-distributed analytical error [*Deino and Potts*, 1992]. A broad 4 to 8 Ma age population dominates the signal (Figure 9b), while secondary 10 to 15 Ma and 15 to 20 Ma populations are also evident. Note that the absolute value of probability displayed on the  $y$  axis of our probability plots is dependent upon the age bin size chosen along the  $x$  axis (this bin size is

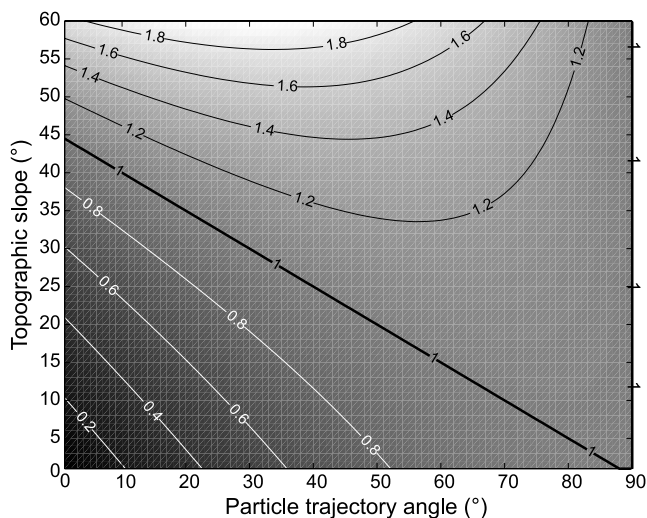


**Figure 7.** Relationship between the topographic slope and particle trajectory angle in determining the volume of material eroded from a DEM cell. The  $X$  and  $Y$  cell dimensions,  $dt$ , and particle speed are set to unity. Note that the surface area of the landscape represented by the  $1 \times 1$  DEM cell varies as a function of slope and that when the particle trajectory is vertical, one unit volume is eroded from the landscape, independently of the topography. As the topographic slope approaches the plane of the particle trajectory, the volume of material eroded approaches zero because material is advected parallel to the slope.

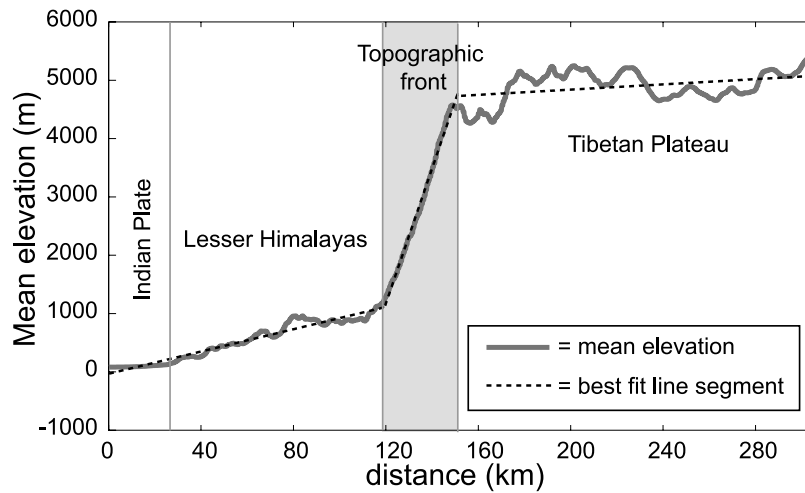


**Figure 8.** Three linear segments (dashed lines) used as a proxy for the regional slope and the steady state topographic profile, taken from a transect normal to the strike of the orogen. The mean elevation, averaged over the ~130 km by 0.6 km swath, is shown by the thick gray line (Figure 1).

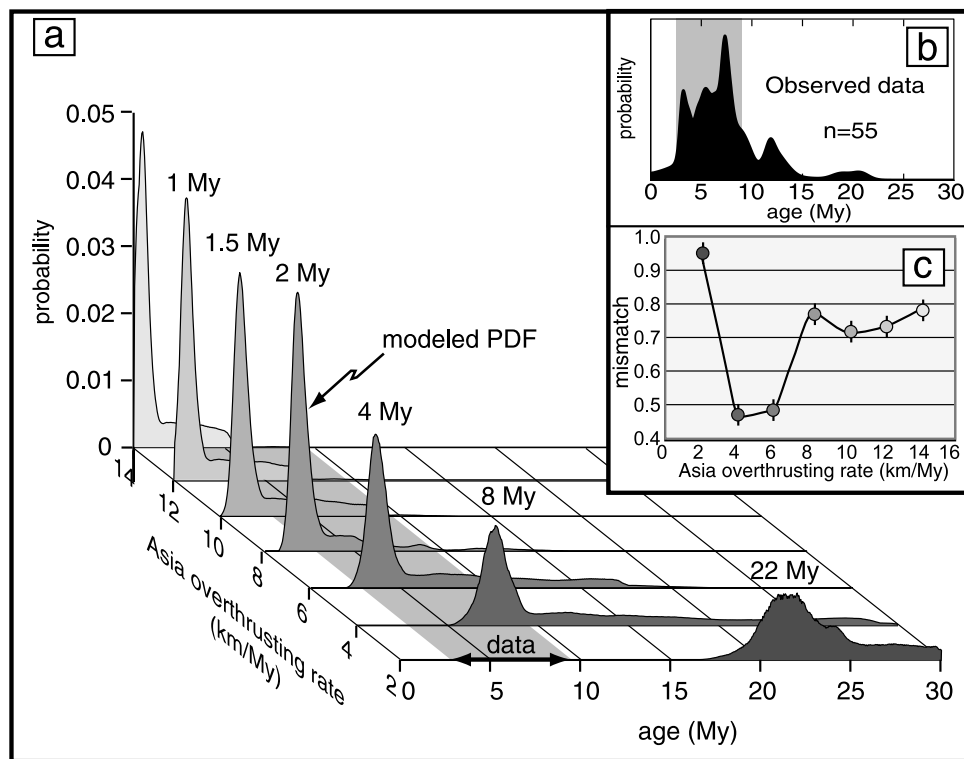


**Figure 9.** (a) Effects of partitioning the convergence rate between India and Asia as represented in the modeled detrital cooling-age signals. The age signals are represented by probability density functions (PDF) and represent the reset age signal from the width of the study area (Figure 1). The overthrusting rate varies between 2 and 14 km Myr<sup>-1</sup> for Asia, keeping the total convergence rate (20 km Myr<sup>-1</sup>) and all else constant. The gray band (labeled “data”) represents an approximate range of the most frequently occurring ages in the observed data PDF. (b) PDF of the observed detrital muscovite ages (S-24 from Brewer *et al.* [2006]). The sample was collected from 200 m upstream of the confluence of the Marsyandi and Trisuli rivers (white dot in Figure 1). Data are smoothed with a 2-Myr scrolling window. (c) Mismatch between the model PDF and the observed PDF of ages (Figure 9b). Lowest mismatch occurs for an Asian overthrusting rate between 4 and 6 km Myr<sup>-1</sup>.

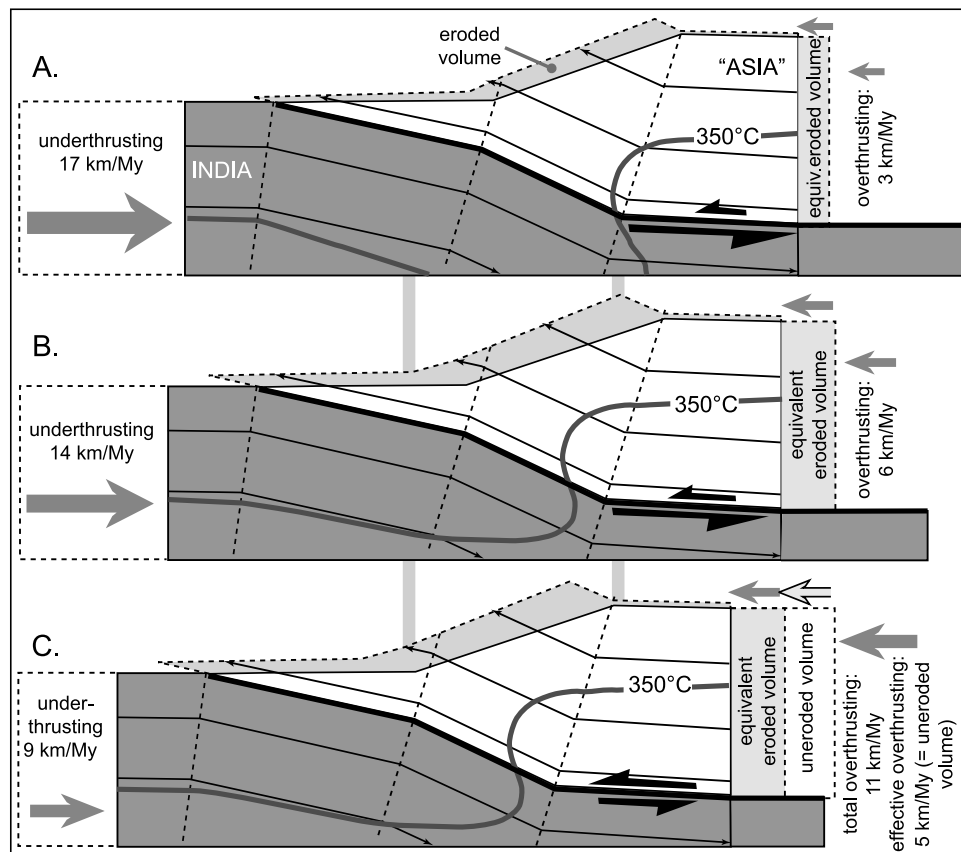


**Figure 10.** Relationship between partitioning of convergence ( $20 \text{ km Myr}^{-1}$ ) into an underthrusting “India” and an overthrusting “Asia” plate, thermal structure, and spatial variations in eroded volumes. Overthrusting is either fully (Figures 10a and 10b) or partially (Figure 10c) compensated by erosion. In all cases, strong spatial variations in erosion at the surface (light gray) occur as a function of the angle between the ramp and the surface, such that (1) large contrasts in cooling ages would be expected across the orogenic surface and (2) no single erosion rate adequately describes the pattern of erosion. (a) Underthrusting of  $17 \text{ km Myr}^{-1}$  and erosionally compensated overthrusting at  $3 \text{ km Myr}^{-1}$ . Rapid underthrusting of the cold Indian plate perturbs the  $350^\circ\text{C}$  isotherm downward. (b) Erosionally compensated overthrusting at  $6 \text{ km Myr}^{-1}$  bringing the  $350^\circ\text{C}$  isotherm closer to the surface. (c) Plot with only  $6$  of  $11 \text{ km Myr}^{-1}$  of overthrusting compensated by erosion of the hanging wall. Whereas the topography shifts  $5 \text{ km Myr}^{-1}$  toward the underthrust plate, the thermal structure is identical to that defined for only  $6 \text{ km Myr}^{-1}$  of overthrusting, all of which is erosionally compensated (Figure 10b). Gray vertical bars provide a reference frame to indicate a left shift of topography at  $5 \text{ km Myr}^{-1}$  between Figures 10b and 10c.

constant in all plots to allow the direct comparison of relative probability).

#### 4. Himalayan Kinematics and Controls on Cooling Ages

##### 4.1. Kinematics: Asian Overthrusting and Erosion Rates

[40] Geodetic studies suggest that the convergence rate of India with southern Tibet ranges from  $13$  to  $21 \text{ km Myr}^{-1}$  [Bilham *et al.*, 1997; Wang *et al.*, 2001; Juanne *et al.*, 2004] and geologic studies in the Himalayan foreland [Lavé and Avouac, 2000] yield well-defined convergence rates averaging  $\sim 20 \text{ km Myr}^{-1}$  over the past 9 kyr. We therefore assign a rate of  $20 \text{ km Myr}^{-1}$  to represent the Indo-Tibetan convergence, but need to partition this between Indian underthrusting and Asian overthrusting. For this model,

the intersection of the Main Himalayan Thrust decollement with surface topography (decollement/surface singularity (DSS), Figure 3) is our reference frame; this theoretical point is independent of how total convergence is partitioned between the two plates.

[41] Notably, in the absence of erosion, no difference exists between the overthrusting and underthrusting: once isostasy is taken into account, they result in the same thermal structure (compare Figures 10b and 10c). Our model, however, assumes that material added to the system as a result of overthrusting is balanced by an equal amount of erosion at the front of the overthrust plate. Conceptually, this is equivalent to holding the landscape surface fixed and removing all rock in the overthrust plate that passes through that surface. The thermal structure of both plates therefore will vary as a function of the rate of overthrusting, because it is directly correlated with the magnitude of erosion.

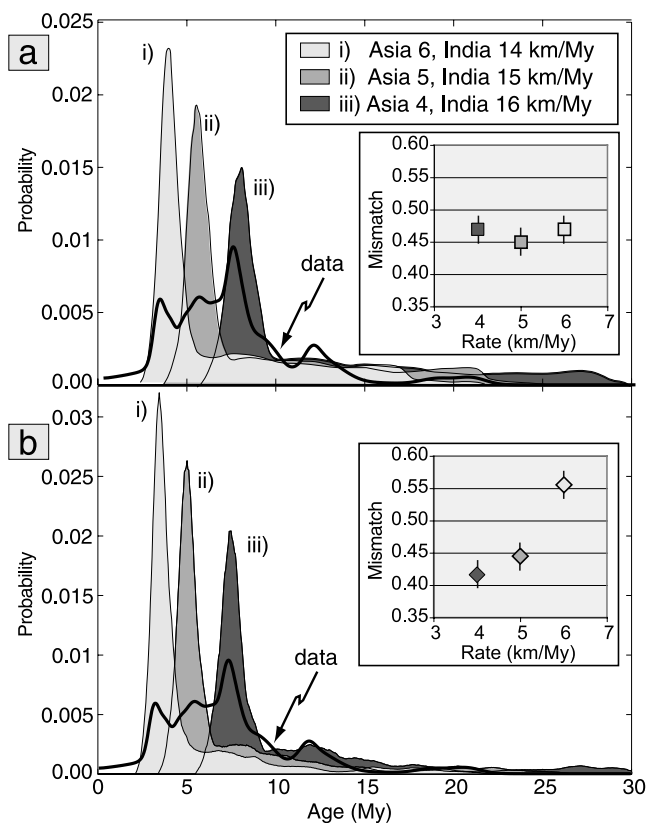


**Figure 11.** (a) Detrital cooling age signal from the entire topographic swath (Figure 1) compared against the sample from the mouth of the Marsyandi (solid black line). Asian overthrusting rates of 4 to 6 km yr<sup>-1</sup> mimic the general pattern of observed detrital data. The PDF generated with Asia is 5 km Myr<sup>-1</sup> and with India is 15 km Myr<sup>-1</sup> (model ii) displays a slightly better fit to the data PDF. (b) The same results as Figure 11a but corrected for the age signal generated specifically from the Marsyandi basin. Note that the peak probabilities are enhanced in the model prediction, while the older tails have diminished importance. Insets show mismatches between modeled and observed data. The best match of all six model occurs for an overthrusting rate of 4 km Myr<sup>-1</sup> (Figure 11b, model ii) but is statistically indistinguishable from a rate of 5 km Myr<sup>-1</sup>.

Partitioning of the remaining convergence (that which is not compensated by erosion) into overthrusting or underthrusting has no additional effect on thermal structure. Therefore, for the sake of simplicity, we assign to the underthrusting Indian plate all convergence that is not erosionally compensated. We choose to use the term “overthrusting rate”, rather than erosion, to indicate the rate at which material enters the model and is removed from the hanging wall, thereby maintaining mass balance. The rate at which material moves vertically toward the topographic surface varies as a function of ramp angle, such that the erosion rate varies spatially in the overthrusting plate and no single value can be assigned to it (Figure 10). Because partitioning of convergence into underthrusting and erosionally compensated overthrusting affects the calculated thermal and velocity structure of the system, it modulates the predicted

cooling ages. Consequently, this partitioning becomes a primary unknown, yet testable, variable.

[42] Simulations indicate that detrital cooling ages are sensitive to the amount of relative convergence, over geologically reasonable rates, that is removed by erosion (Figure 9). At steady state, erosionally compensated overthrusting rates of  $\geq 10$  km Myr<sup>-1</sup> of Asia result in very young age populations with peak probabilities representing ages of  $< 3$  Myr. The detrital cooling-age signal is more sensitive to slow overthrusting rates of Asia with commensurate erosion (Figure 9). With 4 km Myr<sup>-1</sup> of overthrusting, the peak probability occurs between 5 and 10 Myr, whereas if the overthrusting rate decreases to 2 km Myr<sup>-1</sup>, the peak probability shifts markedly to 20 to 25 Myr. Overall, slowing the rate of erosionally compensated Asian overthrusting broadens the range of detrital ages predicted both for the peak probability and the overall age signal; the older age “tails” lengthen significantly with slower rates (Figure 9).

[43] To assess how much of the convergence is expressed as erosion of the Asian plate, we examine the statistical mismatch [Brewer *et al.*, 2003] between the predicted age distribution for different overthrusting rates with the observed age distribution for the Marsyandi River detrital sample. The mismatch calculation does not take into account empirical errors that will produce differences between the modeled PDF and data, but is sufficient to broadly define those models that produce the best results. This comparison yields a key result: the lowest mismatch for overthrusting rates that are erosionally compensated lies between 4 and 6 km Myr<sup>-1</sup> because the predicted detrital ages yield the greatest overlap with the peak probability in the data (lower inset, Figure 9). This narrow window of acceptable rates is emphasized by direct comparisons of the observed data with model scenarios for Asian overthrusting rates of 4, 5, and 6 km Myr<sup>-1</sup> (Figure 11a). Although the best model fit to the data uses 5 km Myr<sup>-1</sup> of Asian overthrusting, the mismatches to the observed data for these three models are statistically indistinguishable (inset, Figure 11a). An overthrusting rate of 5 km Myr<sup>-1</sup> above an 18° ramp yields vertical particle trajectories of  $\sim 1.5$  km Myr<sup>-1</sup>: a rate similar to the average vertical erosion rate ( $1.9 \pm 0.3$  km Myr<sup>-1</sup>) estimated for the Marsyandi’s Greater Himalayan tributary catchments with a model that ignores lateral advection [Brewer *et al.*, 2006]. The model results clearly illustrate that increasing the rate of erosionally compensated overthrusting (Figure 12) produces younger age populations by (1) increasing the rate at which rock moves between the closure temperature and the surface and (2) deflecting the closure isotherm toward the surface by advection of hot rock mass (Figure 12b). In contrast, increasing the rate of underthrusting cools the system by more rapid subduction of relatively cold continental plate (Figure 12a) and hence subduing the effects of warming due to thickened crust and lateral advection of the overthrusting plate.

## 4.2. Angle of Main Himalayan Thrust Ramp

[44] Given the dependence of the thermal state on the kinematic geometry, variations in the decollement geometry impact the model’s cooling-age predictions. Because both the position of the MBT and the depth of the seismicity

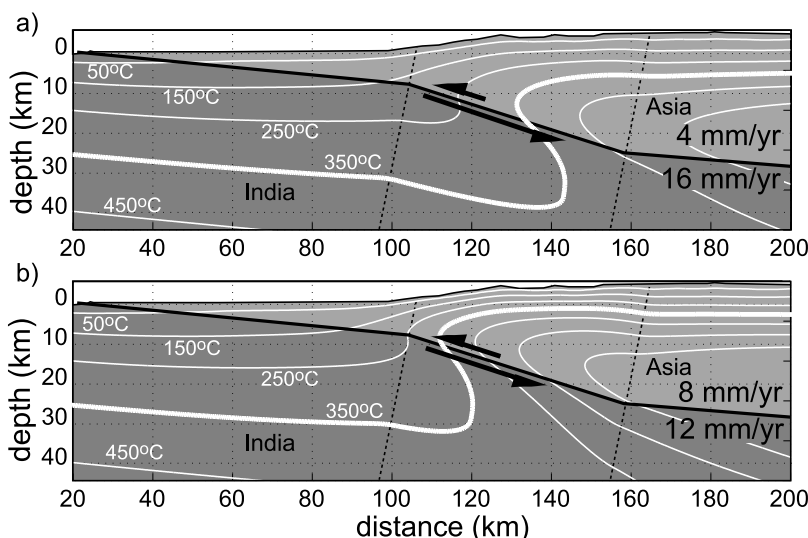


**Figure 12.** Steady state thermal structure with  $20 \text{ km Myr}^{-1}$  of total convergence with (a)  $4 \text{ km Myr}^{-1}$  of erosionally compensated Asian overthrusting and (b)  $8 \text{ km Myr}^{-1}$  of erosionally compensated Asian overthrusting. Note the relative response of the  $350^\circ\text{C}$  isotherm.

interpreted to occur at the top of the Main Himalayan Thrust ramp are relatively well constrained, a primary geometric unknown is the steepness of the ramp underlying the main topographic front. The kinematic model described previously uses a ramp angle of  $18^\circ$  to approximate the interpreted dip of the main decollement beneath the Himalaya [Schelling and Arita, 1991; Pandey et al., 1995; Cattin et al., 2001; Lavé and Avouac, 2001]. To explore the interplay between the ramp angle, overthrusting rate, and predicted cooling ages, four additional scenarios were modeled (Figure 13): two utilize the “best fit” convergence partitioning ( $5 \text{ km Myr}^{-1}$  to Asia and  $15 \text{ km Myr}^{-1}$  to India) with either a steep or gentle ramp; one specifies a steep ramp and slower Asian overthrusting ( $4 \text{ km Myr}^{-1}$ ); and one combines the gentler ramp angle with faster ( $6 \text{ km Myr}^{-1}$ ) overthrusting. The lateral position of the ramp inflection point on the northern end was considered fixed because, as described above, we have assumed a link between the Tethyan strata outcrop, surface topography, and an a hypothesized kink bend in the underlying decollement. As a consequence, the depth of the main decollement under the South Tibetan Detachment system for dips of  $13^\circ$  and  $23^\circ$  becomes  $\sim 25 \text{ km}$  and  $\sim 35 \text{ km}$ , respectively, as opposed to the original  $\sim 30 \text{ km}$  constrained by INDEPTH [Nelson et al., 1996].

[45] Examination of the mismatches of model to data (Figure 13a, bottom inset) shows that, for an overthrusting rate of  $5 \text{ km Myr}^{-1}$ , either a steeper or gentler ramp (models i and v, Figure 13a) yields a poorer match to the data. However, a clear trade off does exist between using a slower rate with a steeper ramp (model ii, Figure 13a) or a faster rate with a gentler ramp (model iv, Figure 13a). Given the data fidelity and uncertainties in the comparison to modeled cooling-age distributions, combinations of overthrusting rates of 5 and  $6 \text{ km Myr}^{-1}$  with ramp angles of  $18^\circ$  and  $13^\circ$ , respectively, yield equally good matches to the data.

[46] The observed cooling-age data from the Marsyandi (comprising 55 ages), against which the model outputs are

compared, are themselves an incomplete representation of the spectrum and abundance of actual cooling ages [Amidon et al., 2005b]. Given that multiple age components appear within the observed data (Figure 11), more ages ( $\geq 100$ ) would be needed to obtain a robust representation of the actual distribution of cooling ages. Hence uncertainties exist in the “observed” data, as well as in the geometry of overthrusting and the partitioning of convergence rates. Nonetheless, this suite of models suggests that, if the ramp angle beneath the Higher Himalaya dips anywhere from  $13^\circ$  to  $23^\circ$ , the likely rate of erosionally compensated Asian overthrusting is approximately  $5 \pm 1 \text{ km Myr}^{-1}$ . More accurate constraints on the deformation geometry, the interaction between erosion and tectonics, and more extensive detrital dating would significantly improve the confidence of these results.

#### 4.3. Modeled Marsyandi Valley Detrital Cooling Age Signal

[47] Until now, we have calculated the detrital age distribution from a rectangular swath across the orogen (Figure 1) because when model predictions are compared with observed cooling ages from a stratigraphic sample in a foreland basin, for example, the contributing catchment area at the time of deposition is almost never reliably known, but it can usually be predicted to lie within a broader region. A sand sample collected from a modern riverbed, however, is actually an integration of points contained within a known upstream catchment area: the distribution of probability within a basin cooling-age PDF will be controlled by the morphology of the present-day basin in relation to the distribution of bedrock cooling ages. With GIS software, the spatial extent of the area draining to any point in the river network can be calculated from a DEM and used as a template to extract the areal distribution of cooling ages. Once corrected for spatial variations in erosion rate, via equation (1), the integrated cooling-age signal can be determined for the specific drainage basin.

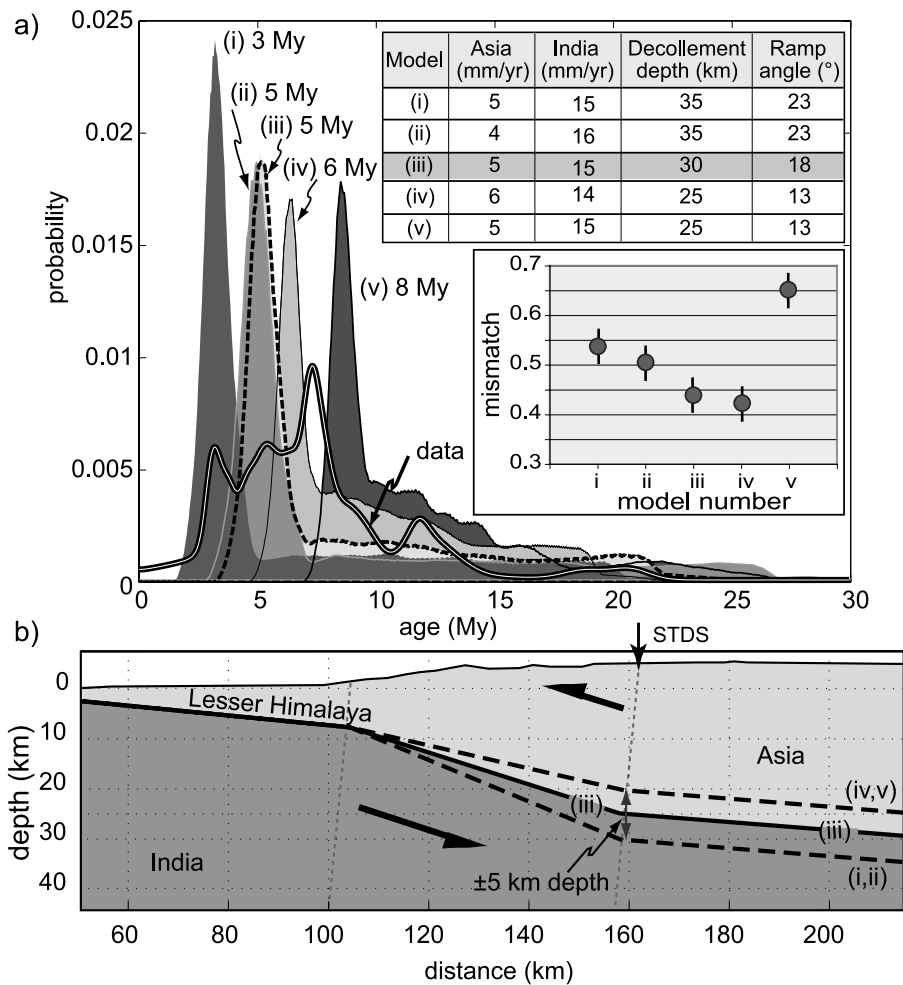


**Figure 13.** (a) Distribution of cooling ages derived from different ramp geometries and Asian overthrusting rates. PDF models i and ii are associated with a steeper  $23^\circ$  ramp (illustrated in Figure 13b, ramp geometry (models i and ii)] with 5 and 4 km  $\text{Myr}^{-1}$  assigned to Asian overthrusting, respectively. PDF model iii, outlined by the dashed line, indicates the age PDF using the original ramp geometry. PDF models iv and v use a shallower geometry (illustrated in Figure 13b, ramp geometry (models iv and v)) with 6 and 5 km  $\text{Myr}^{-1}$ , respectively, assigned to overthrusting of southern Tibet. The data curve represents detrital Marsyandi ages from *Brewer et al.* [2006]. (b) Ramp slopes and geometries (models i/ii, iii, and iv/v) for results in Figure 13a.

[48] Using this methodology, we can reexamine our previous results using the specific drainage area of the Marsyandi River (Figure 11b). The results show that, in comparison to the rectangular swath (Figure 11a), populations of the most probable ages are enhanced when correcting for the drainage area, with the peaks of each distribution shifting to slightly younger ages and older age populations becoming more subdued. This variation occurs because, in comparison to the general swath represented by the model, the Marsyandi catchment contains proportionately more area on the southern flank of the Greater Himalaya that is dominated by younger ages. Similarly, the observed distribution of older ages is better matched by the model output for the Marsyandi catchment alone, rather than for the entire swath. Because the peak probabilities of younger ages are more dominant, however, the mismatch to the observed data

only improves slightly and only for the 4 and 5 km  $\text{Myr}^{-1}$  overthrusting rates (Figure 11b).

#### 4.4. Effects of Lithology

[49] All results thus far implicitly assume a uniform distribution of the thermochronometer (muscovite) across the catchment area. Clearly this is not true in the Himalaya, which contains lithologies as diverse as carbonate mudstones and granites. The volumetric contribution that a lithology makes to the cooling-age signal is dependent upon the abundance of thermochronometer (within the appropriate size fraction) per unit volume of material eroded. For our purposes, the specification of a correct size fraction is an analytical constraint: *Brewer et al.* [2003, 2006] use a grain fraction of 500 to 2000  $\mu\text{m}$  to ensure that individual muscovite grains contain enough radiogenic  $^{40}\text{Ar}$  to detect. Whereas using bedrock sampling or mapping to determine

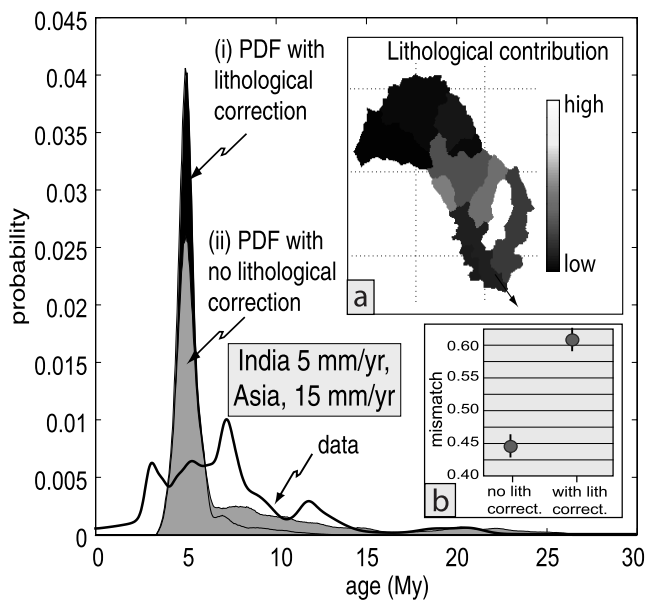


**Figure 14.** Comparison of the computed distribution of detrital cooling ages using, model i, a lithological correction and, model ii, no lithological correction factor. Strong spatial variation in the lithological correction factor over the Marsyandi basin (inset a), taken from the point counting results of *Brewer et al.* [2006]. In this case, the lithologic correction increases the model-data mismatch (inset b).

the abundance of a target mineral is impractical over large areas, point counting detrital samples can readily define the abundance of muscovite in individual tributaries. We use the point counting data from *Brewer et al.* [2006], and for tributaries not sampled in that investigation assign abundance values based on the geology and frequencies from surrounding basins. The outcome is a lithological correction factor for each individual tributary basin that, when combined with the erosion rate and cooling-age maps, produces a refined synthetic cooling-age signal for the basin mouth.

[50] Although many past interpretations of detrital cooling ages assume a uniform distribution of the target mineral(s), point counting in the Marsyandi catchment revealed up to 100-fold differences in muscovite abundances among tributary catchments [*Brewer et al.*, 2006]. Hence a correction of predicted detrital contributions from each tributary should produce a better fit to the observed data. The PDF (Figure 14, curve i) that includes a lithological correction (Figure 14, curve ii), however, produces a worse fit (Figure 14, inset b) than did the PDF predicted using a uniform distribution of thermochronometer (Figure 14, curve ii). The lithologically corrected PDF tends to overpredict younger ages, whereas the >6 Ma age population observed in the data becomes even more underrepresented. This might be due to the spatial resolution of our point counting data: our approach assumes a uniform distribution of thermochronometer within each tributary catchment, whereas heterogeneity is likely, especially in contrasting litho-tectonic zones. For example, tributaries were sampled just upstream of their junction with the Marsyandi River, yet those to the south of the Main Central Thrust typically span both Greater Himalayan and Lesser Himalayan sequences. Where avail-

able, point counting commonly predicted at least twofold differences in muscovite abundance between these two zones [*Brewer et al.*, 2006] that are not differentiated in the analysis here. Such limitations may account for the poorer match when lithology is considered. The general lithological correction technique presented above, however, should produce improved results in areas with better lithological constraints, or in areas with dramatic contrasts in the fraction of thermochronometer.

## 5. Discussion

### 5.1. Modeling

[51] We have presented a modeling technique for predicting the distribution of cooling ages in sediment samples from orogenic rivers. The use of a kinematic-and-thermal framework, in conjunction with the topography, drainage basin morphology, and lithological characteristics of the bedrock, represents a new approach that can help calibrate and test models of orogenic evolution and erosion. Combining the 90-m DEM with the thermal-and-kinematic model helps overcome three major problems of many geochronological models: (1) the assumption of flat isotherms, (2) the variation of bedrock cooling ages with elevation, and (3) the effect of nonvertical rock advection. These are solved simultaneously, as an integral part of the model. The assumption of flat isotherms is replaced by a thermal model that accounts for perturbations caused by (1) the long-wavelength, strike-normal topography and (2) the advection of rock through the system. The variation of bedrock cooling ages with elevation can be more accurately predicted with the calculated relationship between the topography and thermal structure: assumptions of linear and vertical age gradients are no longer required. The effects of lateral velocity fields are already incorporated into the thermal model, and the variation of bedrock cooling ages with position in the landscape is a function of the trajectory of individual rock particles through the orogen.

[52] In this study, we have illustrated this new approach using a simplified model of Himalayan tectonics to predict the distribution of detrital muscovite cooling ages observed at the mouth of the Marsyandi River drainage basin. Despite both the simplicity of the single-decollement model and the many uncertainties in the kinematic and thermal parameters, the results reflect the major attributes of the observed data. In all models, we assume a topographic steady state and consider only that component of overthrusting that is balanced by erosion, because the orogenic thermal structure is otherwise insensitive to the rate of overthrusting, if the total convergence rates are fixed. Various scenarios allow us to examine the effects of (1) changing the ramp geometry of the major decollement and (2) varying the partitioning of Indo-Asian convergence and the consequent erosion of the overthrust plate (Figure 3). Because a trade-off exists between the erosionally compensated overthrusting rate and ramp angle (steeper ramp and slower overthrusting versus gentle ramp and faster overthrusting), several combinations produce acceptable matches to the observed data. Within the likely range of ramp geometry and convergence partitioning, approximately  $5 \pm 1 \text{ km Myr}^{-1}$  is the predicted value for sustained, erosionally compensated, late Cenozoic overthrusting by Asia.

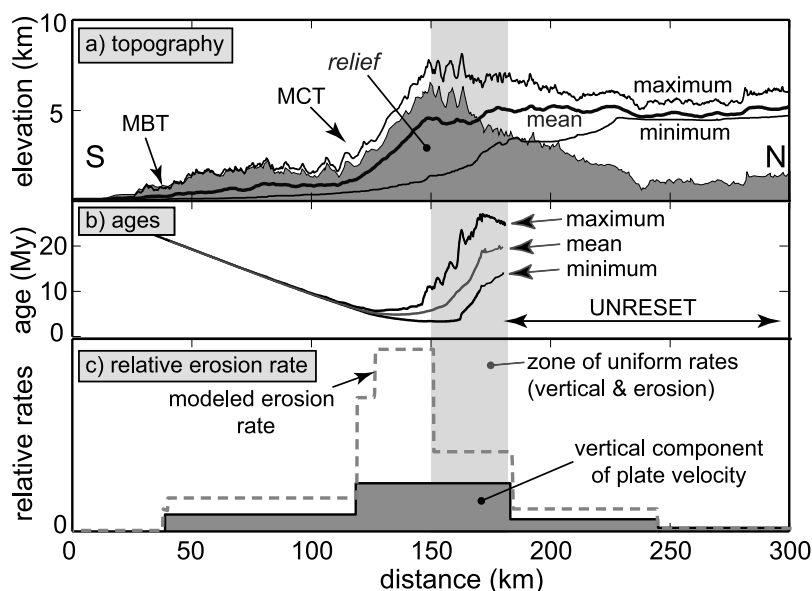


**Figure 15.** Transects illustrating (a) topography and relief, (b) predicted cooling ages from our model, and (c) a comparison between relative vertical erosion rates predicted from ramp geometry and our modeled rates (which are a function of the trajectory of rock particles in relation to the averaged topography). The convergence was partitioned into  $5 \text{ km Myr}^{-1}$  of erosionally compensated Asian overthrusting and  $15 \text{ km Myr}^{-1}$  of Indian underthrusting. The approximate modern locations of the modern MCT and MBT are shown in Figure 15a. The vertical gray bar is a zone of predicted uniform erosion rate (Figure 15c). Note that despite uniform vertical velocity between 120 and 180 km, the modeled erosion rate is much higher in the south due to the steeper southward slope of the mean topography. Similarly, the range of predicted ages is  $>20 \text{ Myr}$  across a zone of uniform erosion rate due to effects of relief, surface slope, and particle trajectories. Notably, the smallest range of predicted cooling ages (Figure 15b) corresponds with the highest relief (Figure 15a): the opposite of expectations for age distributions where rocks only move vertically toward the surface.

[53] Throughout this model and similar to other bedrock cooling models for the Himalaya [e.g., Jamieson *et al.*, 2004], we have assumed the commonly cited closure temperature of  $350^\circ\text{C}$  for muscovite. Given the mean cooling rate in the model, an average closure temperature of  $380^\circ\text{C}$  could be more appropriate [Dodson, 1973]. On the basis of the modeled variations in rates of cooling in this study,  $\sim 90\%$  of our ages would be predicted to have closure temperatures of  $380^\circ \pm 10^\circ\text{C}$ . By ignoring such rate-dependent variations, we introduced an additional uncertainty into the calculated mismatches. The magnitude of this effect, however, is modest compared to other uncertainties in the model. For example, the most rapidly cooled rocks in the model ( $14 \text{ km Myr}^{-1}$  of overthrusting and erosion, Figure 9), would be most affected by use of a low closure temperature, but utilization of a higher closure temperature would only shift the predicted mean age  $\sim 0.1 \text{ Myr}$  and would have little impact on the calculated mismatch to the data. Our interpretations of which overthrusting rates or kinematic geometry provide the best matches to the data would be unchanged, if a nonuniform closure temperature had been incorporated.

[54] We have assessed the agreement between various models and the observed data by comparing the fractional mismatch between their associated PDFs [Brewer *et al.*, 2003]. Whereas pronounced differences in the magnitude of mismatch exist among some models (e.g., Figure 9), no model has  $<40\%$  mismatch. These mismatches are primarily

due to the apparent overprediction of the abundance of young cooling ages in most model runs and to the omission of empirical grain age errors in the model PDFs. Although a smaller mismatch could be achieved by tuning the model using more complex ramp geometries and variable overthrusting rates, few data exist to further constrain these variables. Additional possible explanations for these persistent mismatches include (1) violations of the assumption of a thermal steady state over the duration of the modeled interval and (2) an observed age distribution that does not accurately reflect the actual cooling age distribution. If, for example, the rate of erosion had accelerated in the last few million years, the model could correctly predict the young cooling ages, but would underpredict the residuum of older ages that would be derived from the highest topography or regions with the longest path length from the closure isotherm to the surface. Indeed, apatite fission track dates that average  $\sim 0.5 \text{ Ma}$  for bedrock samples along the Marsyandi valley in the Greater Himalaya [Burbank *et al.*, 2003] require Quaternary cooling rates approaching  $300^\circ\text{C Myr}^{-1}$  and would support an interpretation of accelerated rates of cooling and erosion in the past 1 to 2 Myr. Our observed data PDF comprises only 55 ages. Sampling statistics of complex distributions of actual ages [Amidon *et al.*, 2005b; Anderson, 2005] suggest persistent mismatches of  $\geq 20\%$ , even when 100 ages are drawn from and then matched against a known age distribution.

[55] To illustrate some of the differences between our approach and traditional thermochronology, we examine the predictions of our optimal model along a strike-normal transect (Figure 15). The predicted bedrock cooling ages (Figure 15b) increase both northward over the topographic front and southward over the Lesser Himalaya as a function of particle trajectory (Figure 2). We can compare the distribution of ages to (1) the erosion rate predicted from our model of erosion rate (equation (1)) and (2) that predicted using only the vertical component of the overthrusting vector (Figure 15c). The former predicts much higher volumes of rock eroded from the topographic frontal region, whereas the latter predicts uniform volumes eroded across broad swaths of the orogen. This contrast occurs because, with lateral advection, the erosion rate is a sensitive function of both ramp angle and of topographic slope and orientation, whereas the vertical component depends only on ramp angle.

[56] Both models, however, suggest significant variations in bedrock cooling age across modeled zones of equal erosion. Within a zone for which both models predict uniform erosion (shaded region in Figure 15), the modeled cooling ages vary from a minimum of  $\sim 3$  Myr to a maximum of  $\sim 28$  Myr. This range has important implications because traditional thermochronological approaches, assuming vertical erosion and horizontal isotherms, could interpret such cooling rates ( $120^\circ\text{C Myr}^{-1}$  versus  $12^\circ\text{C Myr}^{-1}$ ) to represent up to tenfold differences in relative erosion rates, instead of the actual uniform rate. Furthermore, the mean cooling ages across this zone of uniform erosion vary by  $\sim 15$  Myr, ranging from 5 to 20 Ma (Figure 15b). This striking difference is a consequence of where particle paths within the orogen intersect the  $350^\circ\text{C}$  isotherm: older mean cooling ages represent rocks that cooled and moved to the surface on a gently inclined trajectory beneath the Tibetan Plateau, whereas younger ages correspond with rocks that cooled within the Greater Himalaya and moved to the surface on a much steeper trajectory. The impact of lateral advection on cooling ages increases in importance as the rate of lateral movement approaches or exceeds the vertical rates, i.e., for ramp angles  $<45^\circ$ , as is common in most convergent orogens. Our model results emphasize that, when cooling-rate studies are used as a proxy for erosion, the effects of both lateral advection and relief need to be integrated into the analysis whenever possible, especially in convergent orogenic belts [Batt and Brandon, 2002; Batt and Braun, 1999; Willett and Brandon, 2002].

[57] Notably, the correspondence between the range of cooling ages and topographic relief (Figure 15) is markedly different than that predicted for “vertical relief sections”. Within a zone of uniform erosion in vertical motion models, the greatest topographic relief should correspond with the largest range of cooling ages. Whereas this could also be true for a lateral advection model, our results predict just the opposite for the central Himalaya: the smallest range of ages corresponds with the greatest relief (Figure 15). On average, the largest range of cooling ages is found north of the high Himalayan peaks where the difference between the shortest and longest particle pathways between the valley bottoms and summits is maximized.

[58] Some verification of the model can be undertaken by comparing the predicted range of ages from a particular part of the orogen (Figure 15b) with observed ages from that area. For example, the model predicts ages ranging from  $\sim 10$  to 25 Ma in the region of the north of the highest peaks, and observed detrital ages for that region (sample A in Figure 16) display a range from  $\sim 9$  to 22 Ma [Brewer *et al.*, 2006]. Closer to the MCT, the model predicts both younger ages and a more restricted range of ages. Data from three tributary catchments that straddle the MCT (samples x, y, z in Figure 16) record ages primarily between 2 and 10 Ma [Brewer *et al.*, 2006]. The model also suggests that the preponderant zone of erosion will occur on the southern flank of the Himalaya (Figure 15c). Such erosion should produce a significant influx of young cooling ages from this part of the orogen. In fact, the young ages emerging from catchments on the southern flank of the range (samples x, y, z in Figure 16) appear to largely overwhelm the older detrital ages from the upstream samples, as seen in the detrital sample at the mouth of the Marsyandi (sample C in Figure 16). Further testing of the model could involve extracting specific tributary catchments from the DEM and comparing the PDFs of modeled ages from these catchments with observed ages from the same catchment. Such a test is beyond the scope of the present paper, but clearly the observed detrital ages are consistent with the spatial trend in ages predicted by the model.

## 5.2. Stratigraphic Record

[59] One major motivation for trying to understand how a cooling-age signal is created is that, in addition to testing numerical models of modern tectonics, dating detrital minerals from the stratigraphic record provides a means to constrain orogenic evolution through time [Bernet *et al.*, 2001; Carrapa *et al.*, 2003; Cervený *et al.*, 1998; Najman *et al.*, 1997; White *et al.*, 2002]. Such investigations are often impractical using bedrock thermochronology, because sampling is typically limited to the rocks exposed at the surface today.

[60] This investigation indicates that the foreland cooling-age data should be representative of the orogenic signal providing that a major transverse river is sampled and that the hinterland does not vary widely along strike. For example, when comparing the entire swath (Figure 11a) and the Marsyandi valley (Figure 11b), the overall pattern remains consistent despite minor modifications of the cooling-age signal. Given the analytical uncertainties in single-crystal dating of Late Cenozoic basin sediments, small changes in the areal extent of the drainage system through time should result in insignificant changes in the observed age spectrum. Whether temporal changes in topographic characteristics, drainage basin shape, and lithological contribution could be extracted from the geological record would depend upon the sensitivity of the thermochronometer and the number of grains dated from the detrital sample [Brewer *et al.*, 2003; Amidon *et al.*, 2005b; Anderson, 2005]. In contrast, major changes in ramp geometry or the erosionally compensated overthrusting rate should be detectable. For example, doubling of the overthrusting rate is predicted to have a profound effect on the distribution of cooling ages (Figure 9) and should be readily observable in the detrital record. To extract maximum information, however, two

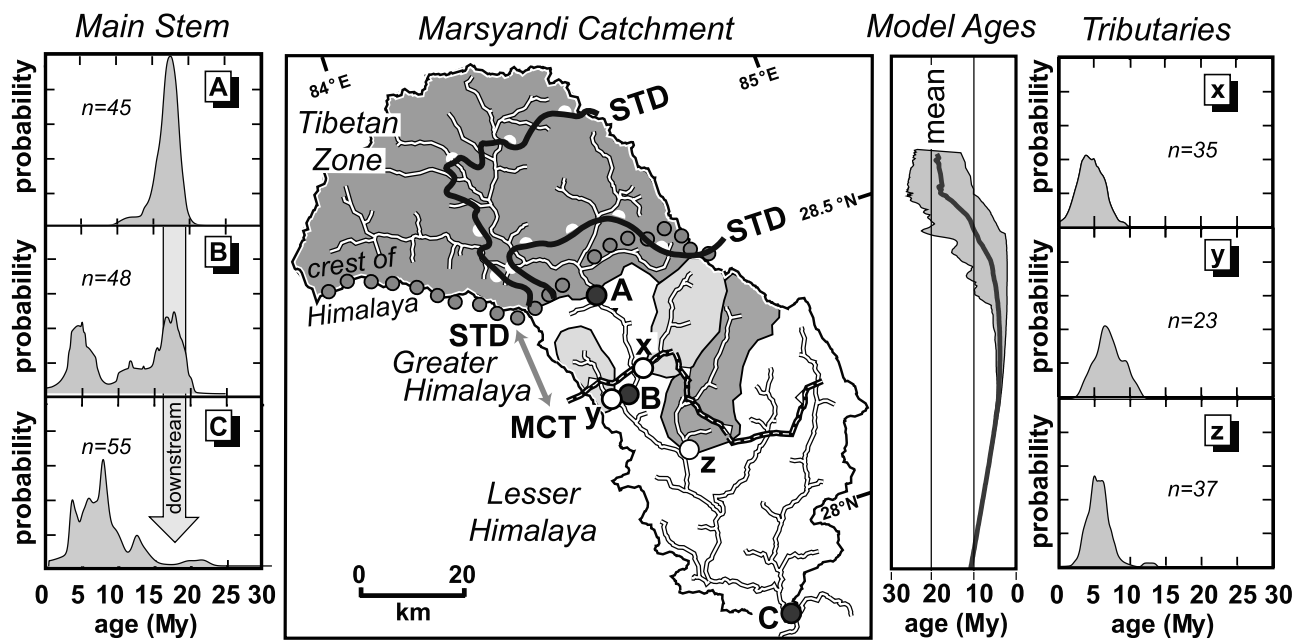


**Figure 16.** Observed detrital cooling ages and modeled bedrock cooling ages in the Marsyandi catchment. Map indicates major structures, lithologic subdivisions, and locations of detrital samples. Samples A, B, and C lie along the Marsyandi main stem, whereas samples x, y, and z come from the mouths of tributaries. The modeled ages are those calculated for this region with an erosionally compensated overthrusting rate of  $5 \text{ km Myr}^{-1}$  (Figure 15b). In accordance with the model age predictions, the northern main stem sample A comprises older ages, whereas samples from tributaries to the south have younger ages and a generally smaller range of ages. The main stem samples show a downstream trend toward younger ages and a loss of significant numbers of older ages: a trend consistent with the predictions both of the modeled ages and of the higher erosion on the southern flank of the Himalaya (Figure 15c). Observed cooling ages are from *Brewer et al.* [2006]. MCT, Main Central Thrust; STD, South Tibetan Detachment.

guidelines should be followed. The modern detrital cooling-age signal should be calibrated to the modern geodynamics in order to understand how the age signal is created, and sampling of the stratigraphic record should be as dense as practical with respect to time in order to define gradual versus abrupt changes and to help discriminate among different types of events, such as a major river capture versus increased rates of erosion.

[61] Many detrital dating studies have focused on changes in lag times as proxies for temporally varying erosion rates within an orogen [e.g., *Bernet et al.*, 2001; *Carrapa et al.*, 2003]. These analyses have typically extracted component age peaks from a distribution [*Brandon*, 2002] and compared them through time. The methodology utilized here suggests that a richer signal can potentially be extracted from such detrital data. In circumstances in which fault geometries and times of slip are well known, modeling analogous to that presented here would predict how the detrital cooling signal should evolve through time. When used in conjunction with other detrital data, such as specific provenance indicators, changes in the location and rate of deformation should be discernable through the changing distributions of detrital ages.

### 5.3. Model Improvements

[62] Potential improvements in the modeling and its assessment fall into four categories: refinement of the model

to include further physical inputs and processes; predictions of a suite of outcomes for different thermochronometers; exploration of the effects of uncertainties in the input parameters and the assumptions made; and improvements in the calibration data (observed ages in this case) used to assess the model. In terms of improving the representation of known processes, rather than assume a single closure temperature, variations in closure temperature could be incorporated as a function of cooling rate and grain size [*Dodson*, 1973], although actual grain size variations for various minerals within a source area are commonly unknown. The thermal model could be improved by direct coupling to the topography in three dimensions, so that both along-strike and across-strike topography affect the thermal regime [*Ehlers et al.*, 2001]. An atmospheric lapse rate function should also be included to account for elevation-dependent changes in surface temperature [*Reiners et al.*, 2003]. Such modifications would be particularly important for lower temperature thermochronometers (e.g., [U-Th]/He dating of apatite) for which closure isotherms lie closer to the surface and are strongly influenced by topography.

[63] Second, modeling closure temperatures and cooling ages for combinations of thermochronometers, such as  $^{40}\text{Ar}/^{39}\text{Ar}$  in muscovite and both [U-Th]/He and fission tracks in apatite and zircon, would provide a diverse suite of PDFs for different erosion scenarios and would enable less ambiguous matches to observed data sets. For example,

modeling of two or more thermochronometers with higher and lower closure temperatures could define an acceleration in the rate of cooling or test the predicted minimum duration required to reach a thermal steady state. Reliance on minerals with higher closure temperatures, however, has to be balanced against the assumptions of steady state or kinematic rates. The older the cooling ages, the more likely that rates and topography have changed since the closure temperature was passed by a rock now found at the surface. In order to test model predictions of ages, either individual or combinations of modeled thermochronometers could be extracted from DEM-defined tributaries across an orogen and then compared against observed detrital ages from the same catchments. A robust model should predict spatial trends of ages that are mimicked by observed detrital ages.

[64] Third, many assumptions and simplifications, such as the existence of thermal and topographic steady states or the presence of a single, geometrically simple detachment, underpin the present model. In future work, the impact of these should be explored and more complex input data and controls should be used, as they become available. Removing the thermal steady state assumption and allowing erosionally compensated overthrusting rates to change during a model run might, for example, provide a more realistic thermal evolution, if the many complications related to unknown changes in the surface topography and in the timing of changes in rates could be constrained. For further analysis, reliable field data are important both to define the range of acceptable model inputs and to provide good calibration data.

[65] Although improved knowledge of heat production and thermal conductivity would also be helpful, the geometry of the deformation system is the largest unknown. Balanced cross sections and seismic data can help define more reliable fault geometries. Both the distributed nature of seismicity within many active orogens [e.g., *Seeber et al.*, 1981] and predictions for deformation within critically tapered wedges where differential erosion removes mass in the wedge's internal parts [*Sobel et al.*, 2003; *Wobus et al.*, 2003, 2005] indicate that single decollement models are unlikely to capture the complexity of actual deformation histories [*Pearson and DeCelles*, 2005]. Incorporation of additional fault surfaces with known geometries into models and prediction of cooling ages resulting from slip along them would provide another template against which to assess and interpret observed data. In our model, the overthrusting and underthrusting plates are persistently separated by a single decollement and no material passes across that fault. A model permitting transfer of material from the underthrust to the overthrust plate would be more consistent with the observed accretion from the underthrust plate to the hanging wall of the decollement. Such accretion could explain the presence of unrest ages in the Lesser Himalaya [*Bollinger et al.*, 2004; *Jamieson et al.*, 2004; *Wobus et al.*, 2003].

[66] In the northern reaches of the Marsyandi, recent structural mapping suggests multiple, large-scale folds in the northern Greater Himalaya [*Searle and Godin*, 2003], implying kinematic pathways that are more complicated than our simple fault bend fold model. In the Burhi Gandaki, just east of the Marsyandi, an abrupt discontinuity in muscovite cooling ages occurs ~20 km south of the MCT

and is interpreted as a major MCT footwall thrust [*Wobus et al.*, 2003, 2005]. South of this zone, no Tertiary muscovite cooling ages are reported. Our kinematic model with a single, uniformly dipping ramp extending to the MBT is incompatible with the absence of Tertiary cooling ages in the southern Lesser Himalaya. Although *Brewer et al.* [2006] show that only 2 out of >200 detrital muscovite dates from catchments traversing the Lesser Himalaya in the Marsyandi have cooling ages >30 Ma, it is possible that a Paleozoic age signal from the Lesser Himalaya was undetected due to smaller mica grain sizes that were below our cutoff for measurement. The conflicts in interpretations described above are relevant to the cross-sectional structural geometry of the orogen. Along-strike changes in kinematics add still further complexity to particle paths through the orogen. However, given the difficulty of defining the details of geometric and kinematic variability, simple kinematic models that capture the essence of a system without trying to recreate every detail may be best for providing an understanding of the geological processes and interactions that affect the cooling-age signal.

[67] In the context of comparing modeled age predictions with observed detrital ages, our model does not explicitly incorporate the variability introduced by using observed data sets comprising limited numbers of grain ages (55 used here). Such age distributions almost always incompletely represent the parent distribution from which they were drawn. Rather than comparing observed data, containing  $N$  ages, with the PDF of all ages across the model space, Monte Carlo sampling of  $N$  predicted ages, with appropriate age uncertainties, from the modeled PDF [*Brewer et al.*, 2003; *Ruhl and Hodges*, 2005] and statistical analysis of the Monte Carlo predictions would provide a better basis for assessing model-data mismatches.

[68] Incorporation of spatial changes in the bedrock abundance and grain size of target thermochronologic mineral(s) would improve predictions of how erosion rates convolve with mineralogic abundances to modulate the frequency of cooling ages in a detrital sample. Whereas we accounted for measured spatial changes in mica abundance, we ignored the effect of potential variations in mica grain size. For example, if Lesser Himalayan schists yield abundant, but small micas (<500  $\mu\text{m}$ ), we would have missed these because we only analyzed micas >500  $\mu\text{m}$ .

[69] Fourth, improvements in the quality of the observed data would assist in choosing among diverse model predictions. Rather than assuming that no downstream comminution occurs, tests of attrition could be implemented via comparisons of age distributions for resistant (zircon) versus more abrasion-susceptible (micas, apatite) minerals. Similarly, the grain size dependence of the age signal [*Ruhl and Hodges*, 2005] could be routinely assessed, whereas increasing the number of detrital ages to >100 would produce a more robust PDF for the purposes of comparison.

## 6. Conclusions

[70] Few previous kinematic-and-thermal chronological models have considered either detrital cooling-age signals or the effects of actual topography upon the distribution of cooling ages. In this paper, we have introduced a new method of combining digital elevation models with numer-

ical kinematic-and-thermal modeling to predict spatial variations in bedrock cooling ages. Once corrected for (1) the relative erosion rate and (2) the relative abundance of the mineral utilized as a thermochronometer, the cooling-age signal can be determined for any catchment area. Notably, even in regions overlying a planar thrust ramp, the erosion rate can vary considerably as a function of the angle between the average surface topography and particle trajectories approaching the surface. Because detrital mineral samples are easily collected and dated, and also represent an integration of information from a large spatial area, they provide a good method of rapid testing of increasingly complex numerical simulations. On the other hand, bedrock sampling to provide a comparable suite of observed ages is impractical and may be impossible in high relief and glaciated alpine regions.

[71] A striking model result is the prediction that, even within a zone of uniform erosion in a convergent orogen, a cooling age population can display a broad range of ages. In this study, the youngest and oldest model ages differ by a factor of 9, ranging from 3 to 28 Myr (Figure 15). For models in which rock only moves vertically toward the surface at a uniform erosion rate, the largest range of ages correlates with the largest topographic relief. In contrast, lateral advection of rocks causes the relationship between relief and the range of cooling ages to decouple, and in this particular case study, the smallest range of ages within a zone of uniform erosion occurs where the relief is highest.

[72] We have applied this new methodology to modeling the detrital cooling-age signal of the Marsyandi River in central Nepal. The results illustrate that the distribution of bedrock cooling ages is sensitive to the amount of overthrusting that is compensated by erosion, because this erosion modulates the thermal structure of the orogen. With a single decollement, and the surface outcrop of the MBT representing the modern Main Himalayan Thrust, the detrital cooling age data of Brewer *et al.* [2006] are most closely matched by partitioning the total convergence rate between India and southern Tibet ( $\sim 20$  km Myr<sup>-1</sup>), such that  $\sim 5$  km Myr<sup>-1</sup> of Asian overthrusting is removed by erosion. In the context of the modeled distribution of bedrock cooling ages, a trade-off exists between ramp angle and erosion rates of the overthrust plate. Within reasonable geometrical limits on the ramp, however, the partitioning of the convergence rate can be constrained to approximately  $\pm 1$  km Myr<sup>-1</sup>, given an appropriate thermal structure. The modification of the detrital cooling-age signal by drainage basin shape and distribution of thermochronometer is a secondary effect within the Marsyandi drainage basin.

[73] This study provides insights into how the detrital cooling-age signal reflects the deformation pattern within a collisional orogen. Detrital-mineral thermochronology can provide an efficient way to test ideas of orogenic development, and the methodology introduced here can be combined with many other numerical models to predict the distribution of detrital cooling ages. With better temporal controls on the timing and activity of faults, future kinematic-and-thermal models for the Himalaya would be greatly improved. The effects of topographic deflection of the closure isotherm, particularly important for lower temperature thermochronometers such as apatite fission track and (U-Th)/He dating, could be investigated with fully 3-D

thermal models. The greatest advantage to detrital, as opposed to bedrock, thermochronology is that the stratigraphic record provides a window into the past. Therefore sequential reconstructions of orogenic evolution, once calibrated with the modern detrital cooling-age signal, can be assessed against detailed, quantitative field data derived from foreland basin sediments.

[74] **Acknowledgments.** This work was funded by National Science Foundation grants EAR-9627865, EAR-9896048, and EAR-9909647. The Chevron Corporation also provided financial support. We thank R. Malserversi, C. Guzowski, and T. Ehlers for helpful discussions about the thermal modeling, and K. Hodges and J. Lavé for discussions of Himalayan geology. This manuscript was significantly improved through the comments and questions of K. Whipple, J. Braun, R. Jamieson, and an anonymous reviewer.

## References

- Amidon, W. H., D. W. Burbank, and G. E. Gehrels (2005a), Construction of foreland mineral populations: Insights from mixing of U-Pb zircon ages in Himalayan rivers, *Basin Res.*, *17*, 463–485, doi:10.1111/j.1365-2117.2005.00279.x.
- Amidon, W. H., D. W. Burbank, and G. E. Gehrels (2005b), U-Pb zircon ages as a sediment mixing tracer in the Nepal Himalaya, *Earth Planet. Sci. Lett.*, *235*, 244–260.
- Anderson, T. (2005), Detrital zircons as tracers of sedimentary provenance: Limiting conditions from statistics and numerical simulation, *Chem. Geol.*, *216*, 249–270.
- Barbey, P., M. Brouand, P. Le Fort, and A. Pêcher (1996), Granite-migmatite genetic link: The example of the Manaslu Granite and Tibetan Slab migmatites in central Nepal, *Lithos*, *38*(1–2), 63–79.
- Batt, G. E., and M. T. Brandon (2002), Lateral thinking: 2-D interpretation of thermochronology in convergent orogenic settings, *Tectonophysics*, *349*, 185–201.
- Batt, G. E., and J. Braun (1999), The tectonic evolution of the Southern Alps, New Zealand: Insights from fully thermally coupled dynamical modelling, *Geophys. J. Int.*, *136*, 403–420.
- Beaumont, C., P. Fullsack, and J. Hamilton (1992), Erosional control of active compressional orogens, in *Thrust Tectonics*, edited by K. R. McClay, pp. 1–18, CRC Press, Boca Raton, Fla.
- Beaumont, C., R. A. Jamieson, M. H. Nguyen, and B. Lee (2001), Himalayan tectonics explained by extrusion of a low-viscosity crustal channel coupled to focused surface denudation, *Nature*, *414*, 738–742.
- Beaumont, C., R. A. Jamieson, M. H. Nguyen, and S. Medvedev (2004), Crustal channel flows: 1. Numerical models with applications to the tectonics of the Himalayan-Tibetan orogen, *J. Geophys. Res.*, *109*, B06406, doi:10.1029/2003JB002809.
- Bernet, M., M. Zattin, J. I. Garver, M. T. Brandon, and J. A. Vance (2001), Steady-state exhumation of the European Alps, *Geology*, *29*, 35–38.
- Bilham, R., K. Larson, J. Freymueller, and P. I. Members (1997), GPS measurements of present-day convergence across the Nepal Himalaya, *Nature*, *386*, 61–64.
- Bollinger, L., J. P. Avouac, O. Beyssac, E. J. Catlos, T. M. Harrison, M. Grove, B. Goffé, and S. Sapkota (2004), Thermal structure and exhumation history of the Lesser Himalaya in central Nepal, *Tectonics*, *23*, TC5015, doi:10.1029/2003TC001564.
- Brandon, M. T. (2002), Decomposition of mixed grain-age distributions using BINOMFIT, *On Track*, *24*, 13–18.
- Brewer, I. D., D. W. Burbank, and K. V. Hodges (2003), Modelling detrital cooling-age populations: Insights from two Himalayan catchments, *Basin Res.*, *15*, 305–320.
- Brewer, I. D., D. W. Burbank, and K. V. Hodges (2006), Downstream development of a detrital cooling-age signal: Insights from <sup>40</sup>Ar/<sup>39</sup>Ar muscovite thermochronology in the Nepalese Himalaya, in *Tectonics, Climate, and Landscape Evolution*, edited by S. D. Willett *et al.*, *Spec. Pap. Geol. Soc. Am.*, *398*, 321–338, doi:10.1130/2006.2398(20).
- Brown, L. D., W. Zhao, K. D. Nelson, M. Hauk, D. Alsdorf, A. Ross, M. Cogan, M. Clark, X. Liu, and J. Che (1996), Bright spots, structure, and magmatism in Southern Tibet from INDEPTH seismic reflection profiling, *Science*, *274*, 1688–1690.
- Burbank, D., J. Leland, E. Fielding, R. Anderson, N. Brozovic, M. Reid, and C. Duncan (1996), Bedrock incision, rock uplift and threshold hillslopes in the northwestern Himalayas, *Nature*, *379*, 505–510.
- Burbank, D. W., A. E. Blythe, J. Putkonen, B. Pratt-Sitaula, E. Gabet, M. Oskin, A. Barros, and T. P. Ojha (2003), Decoupling of erosion and precipitation in the Himalayas, *Nature*, *426*, 652–655.

- Burbank, D. W., I. D. Brewer, E. R. Sobel, and M. E. Bullen (2006), Single-crystal dating and the detrital record of orogenesis, *Int. Assoc. Sedimentol. Spec. Publ.*, in press.
- Carrapa, B., J. Wijbrans, and G. Bertotti (2003), Episodic exhumation in the western Alps, *Geology*, *31*, 601–604.
- Catlos, E. J., T. M. Harrison, M. J. Kohn, M. Grove, F. J. Ryerson, C. E. Manning, and B. N. Upreti (2001), Geochronologic and thermobarometric constraints on the evolution of the Main Central Thrust, central Nepal Himalaya, *J. Geophys. Res.*, *106*, 16,177–16,204.
- Cattin, R., G. Martelet, P. Henry, J. P. Avouac, M. Diament, and T. R. Shakya (2001), Gravity anomalies, crustal structure and thermo-mechanical support of the Himalaya of central Nepal, *Geophys. J. Int.*, *147*, 381–392.
- Cerveny, P. F., N. D. Naeser, P. K. Zeitler, C. W. Naeser, and N. M. Johnson (1998), History of uplift and relief of the Himalaya during the past 18 million years: Evidence from sandstones of the Siwalik Group, in *New Perspectives in Basin Analysis*, edited by K. L. Kleinspehn and C. Paola, pp. 43–61, Springer, New York.
- Chen, Q., J. T. Freymueller, Z. Yang, C. Xu, W. Jiang, Q. Wang, and J. Liu (2004), Spatially variable extension in southern Tibet based on GPS measurements, *J. Geophys. Res.*, *109*, B09401, doi:10.1029/2002JB002350.
- Colchen, M., P. LeFort, and A. Pêcher (1986), *Annapurna–Manaslu–Ganesh Himal*, 136 pp., Centre Natl. de la Rech. Sci., Paris.
- Coleman, M. E. (1996), Orogen-parallel and orogen-perpendicular extension in the central Nepalese Himalayas, *Geol. Soc. Am. Bull.*, *108*, 1594–1607.
- Coleman, M., and K. Hodges (1995), Evidence for Tibetan Plateau uplift before 14 Myr ago from a new minimum age for E-W extension, *Nature*, *374*, 49–52.
- Copeland, P., R. Parrish, and M. Harrison (1988), Identification of inherited radiogenic Pb in monazite and its implications for U-Pb systematics, *Nature*, *333*, 760–763.
- Copeland, P., T. M. Harrison, and P. LeFort (1990), Age and cooling history of the Manaslu granite: Implications for Himalayan tectonics, *J. Volcanol. Geotherm. Res.*, *44*, 33–50.
- DeCelles, P. G., G. E. Gehrels, J. Quade, and T. P. Ojha (1998), Eocene-early Miocene foreland basin development and the history of Himalayan thrusting, western and central Nepal, *Tectonics*, *17*, 741–765.
- DeCelles, P. G., G. E. Gehrels, J. Quade, B. Lareau, and M. Spurlin (2000), Tectonic implications of U-Pb zircon ages of the Himalayan orogenic belt in Nepal, *Science*, *288*, 497–499.
- Deino, A., and R. Potts (1992), Age-probability spectra for examination of single-crystal  $^{40}\text{Ar}/^{39}\text{Ar}$  dating results: Examples from Olorgesailie, southern Kenya Rift, *Quat. Int.*, *13/14*, 47–53.
- DeMets, C., R. G. Gordon, D. F. Argus, and D. Stein (1994), Effect of recent revisions to the geomagnetic reversal time scale and estimates of current plate motions, *Geophys. Res. Lett.*, *21*, 2191–2194.
- Derry, L. A., and C. France-Lanord (1996), Changing riverine  $^{87}\text{Sr}/^{86}\text{Sr}$  and Neogene Himalayan weathering history: Impact on the marine Sr record, *Earth Planet. Sci. Lett.*, *142*, 59–74.
- Dewey, J., J. R. Shackleton, C. Chengfa, and S. Yiyin (1988), The tectonic evolution of Tibet, in *The Geological Evolution of Tibet: Report of the 1985 Royal Society-Academia Sinica Geotraverse of the Qinghai-Xizang Plateau*, pp. 379–413, R. Soc. London, London.
- Dodson, M. (1973), Closure temperature in cooling thermochronological and petrological systems, *Contrib. Mineral. Petrol.*, *40*, 259–274.
- Duvall, A., E. Kirby, and D. Burbank (2004), Tectonic and lithologic controls on bedrock channel profiles and processes in coastal California, *J. Geophys. Res.*, *109*, F03002, doi:10.1029/2003JF000086.
- Edwards, R. M. (1995),  $^{40}\text{Ar}/^{39}\text{Ar}$  geochronology of the Main Central Thrust (MCT) region: Evidence for late Miocene to Pliocene disturbances along the MCT, Marsyangdi River valley, west-central Nepal Himalaya, *J. Nepal Geol. Soc.*, *10*, 41–46.
- Ehlers, T. A., P. A. Armstrong, and D. S. Chapman (2001), Normal fault thermal regimes and the interpretation of low-temperature thermochronometers, *Phys. Earth Planet. Inter.*, *126*, 179–194.
- Ehlers, T. A., and K. A. Farley (2003), Apatite (U-Th)/He thermochronometry: Methods and applications to problems in tectonic and surface processes, *Earth Planet. Sci. Lett.*, *206*, 1–14.
- England, P., and D. McKenzie (1982), A thin viscous sheet model for continental deformation, *Geophys. J. R. Astron. Soc.*, *70*, 295–321.
- England, P., P. LeFort, P. Molnar, and A. Pêcher (1992), Heat sources for Tertiary metamorphism and anatexis in the Annapurna-Manaslu region, central Nepal, *J. Geophys. Res.*, *97*, 2107–2128.
- Ferra, G., B. Lombardo, and S. Tonarini (1983), Rb/Sr geochronology of granites and gneisses from the Mount Everest region, Nepal Himalaya, *Geol. Rundsch.*, *72*, 119–136.
- Fitzgerald, P. G., R. B. Sorkhabi, T. F. Redfield, and E. Stump (1995), Uplift and denudation of the central Alaska Range: A case study in the use of apatite fission track thermochronology to determine absolute uplift parameters, *J. Geophys. Res.*, *100*, 20,175–20,191.
- Fletcher, C. A. J. (1991), *Computational Techniques for Fluid Dynamics*, 420 pp., Springer, New York.
- Gansser, A. (1964), *Geology of the Himalayas*, 289 pp., Wiley-Interscience, Hoboken, N. J.
- Gehrels, G. E., P. G. DeCelles, A. J. Martin, T. P. Ojha, G. Pinhasi, and B. N. Upreti (2003), Initiation of the Himalayan orogen as an early Paleozoic thin-skinned thrust belt, *GSA Today*, *13*, 4–9.
- Gupta, M. L. (1993), Is the Indian Shield hotter than other Gondwana shields?, *Earth Planet. Sci. Lett.*, *115*, 275–285.
- Hansen, F. D., and N. L. Carter (1982), Creep of selected crustal rocks at 1000 MPa, *Eos Trans. AGU*, *63*, 437.
- Harris, N., and J. Massey (1994), Decompression and anatexis of Himalayan metapelites, *Tectonics*, *13*, 1537–1546.
- Harrison, T. M., K. D. McKeegan, and P. LeFort (1995), Detection of inherited monazite in the Manaslu leucogranite by  $^{208}\text{Pb}/^{232}\text{Th}$  ion microprobe dating: Crystallization age and tectonic implications, *Earth Planet. Sci. Lett.*, *133*, 271–282.
- Harrison, T. M., F. J. Ryerson, P. LeFort, A. Yin, O. M. Lovera, and E. J. Catlos (1997), A late Miocene-Pliocene origin for the central Himalayan inverted metamorphism, *Earth Planet. Sci. Lett.*, *146*, E1–E7.
- Harrison, T., M. Grove, L. Oscar, and E. Catlos (1998), A model for the origin of Himalayan anatexis and inverted metamorphism, *J. Geophys. Res.*, *103*, 27,017–27,032.
- Henry, P., X. Le Pichon, and B. Goffé (1997), Kinematic, thermal and petrological model of the Himalayas: Constraints related to metamorphism within the underthrust Indian crust and topographic elevation, *Tectonophysics*, *273*, 31–56.
- Hodges, K. V. (2000), Tectonics of the Himalaya and southern Tibet from two perspectives, *Geol. Soc. Am. Bull.*, *112*, 324–350.
- Hodges, K. V., R. R. Parrish, and M. P. Searle (1996), Tectonic evolution of the central Annapurna Range, Nepalese Himalayas, *Tectonics*, *15*, 1264–1291.
- Hodges, K., C. Wobus, K. Ruhl, T. Schildgen, and K. Whipple (2004), Quaternary deformation, river steepening, and heavy precipitation at the front of the Higher Himalayan ranges, *Earth Planet. Sci. Lett.*, *220*, 379–389.
- Jackson, M., and R. Bilham (1994), Constraints on Himalayan deformation inferred from vertical velocity fields in Nepal and Tibet, *J. Geophys. Res.*, *99*, 13,897–13,912.
- Jackson, M., S. Barrientos, R. Bilham, D. Kyestha, and B. Shrestha (1992), Uplift in the Nepal Himalaya revealed by spirit leveling, *Geophys. Res. Lett.*, *19*, 1539–1542.
- Jamieson, R. A., C. Beaumont, P. Fullsack, and B. Lee (1998), Barrovian regional metamorphism: Where's the heat, in *What Drives Metamorphism and Metamorphic Reactions*, edited by P. J. Treloar and P. J. O'Brien, *Geol. Soc. Spec. Publ.*, *138*, 23–51.
- Jamieson, R. A., C. Beaumont, M. H. Nguyen, and B. Lee (2002), Interaction of metamorphism, deformation and exhumation in large convergent orogens, *J. Meteorol. Geol.*, *20*, 9–24.
- Jamieson, R. A., C. Beaumont, S. Medvedev, and M. H. Nguyen (2004), Crustal channel flows: 2. Numerical models with implications for metamorphism in the Himalayan-Tibetan orogen, *J. Geophys. Res.*, *109*, B06407, doi:10.1029/2003JB002811.
- Juane, F., J.-L. Mugnier, J. F. Gamond, P. LeFort, M. R. Pandey, L. Bollinger, M. Flouzat, and J.-P. Avouac (2004), Current shortening across the Himalayas of Nepal, *Geophys. J. Int.*, *157*, 1–14.
- Koons, P. O. (1989), The topographic evolution of collisional mountain belts: A numerical look at the Southern Alps, New Zealand, *Am. J. Sci.*, *289*, 1041–1069.
- Koons, P. O. (1995), Modeling the topographic evolution of collisional belts, *Annu. Rev. Earth Planet. Sci. Lett.*, *23*, 375–408.
- Kutzbach, J. E., W. L. Prell, and W. F. Ruddiman (1993), Sensitivity of Eurasian climate to surface uplift of the Tibetan Plateau, *J. Geol.*, *100*, 177–190.
- Lavé, J., and J.-P. Avouac (2000), Active folding of fluvial terraces across the Siwaliks Hills, Himalayas of central Nepal, *J. Geophys. Res.*, *105*, 5735–5770.
- Lavé, J., and J.-P. Avouac (2001), Fluvial incision and tectonic uplift across the Himalaya of central Nepal, *J. Geophys. Res.*, *106*, 26,561–26,591.
- Lavé, J., D. Yule, S. Sapkota, K. Basant, C. Madden, M. Attal, and R. Pandey (2005), Evidence for a great medieval earthquake (~1100 A.D.) in the central Himalayas, Nepal, *Science*, *307*, 1302–1305.
- LeFort, P. (1975), Himalayas: The collided range. Present knowledge of the continental arc, *Am. J. Sci.*, *275A*, 1–44.
- Lyon-Caen, H., and P. Molnar (1983), Constraints on the structure of the Himalaya from an analysis of gravity anomalies and a flexural model of the lithosphere, *J. Geophys. Res.*, *88*, 8171–8191.

- Macfarlane, A. M., K. V. Hodges, and D. Lux (1992), A structural analysis of the Main Central Thrust zone, Langtang National Park, central Nepal, *Geol. Soc. Am. Bull.*, *104*, 1389–1402.
- Mancktelow, N. S., and B. Grasemann (1997), Time-dependent effects of heat advection and topography on cooling histories during erosion, *Tectonophysics*, *270*, 167–195.
- Martin, M. A., P. G. DeCelles, G. E. Gehrels, P. J. Patchett, and C. Isachsen (2005), Isotopic and microstructural constraints on the location of the Main Central Thrust in the Annapurna Range, central Nepal Himalaya, *Geol. Soc. Am. Bull.*, *117*, 926–944.
- Mathur, L. P., and G. Kohli (1964), Exploration and development for oil in India, *Proc. World Pet. Congr. Actes Doc. Congres Mondial Pet.*, 633–658.
- McDougall, I., and T. M. Harrison (1999), *Geochronology and Thermochronology by the  $^{40}\text{Ar}/^{39}\text{Ar}$  Method*, 269 pp., Oxford Univ. Press, New York.
- Meigs, A. J., D. W. Burbank, and R. A. Beck (1995), Middle-late Miocene (>10 Ma) formation of the Main Boundary Thrust in the western Himalaya, *Geology*, *23*, 423–426.
- Molnar, P., and P. Tapponnier (1975), Cenozoic tectonics of Asia: Effects of a continental collision, *Science*, *189*, 419–425.
- Nábelek, J. L., J. Vergne, G. Hetenyi, and Hi-CLIMB Team (2005), Project Hi-CLIMB: A synoptic view of the Himalayan collision zone and southern Tibet, *Eos Trans. AGU*, *86*(52), Fall Meet. Suppl., Abstract T52A-02.
- Najman, Y. M. R., M. S. Pringle, M. R. W. Johnson, A. H. F. Robertson, and J. R. Wijbrans (1997), Laser (super 40)  $^{40}\text{Ar}/^{39}\text{Ar}$  dating of single detrital muscovite grains from early foreland-basin sedimentary deposits in India: implications for early Himalayan evolution (1997), *Geology*, *25*, 535–538.
- Nelson, K. D., et al. (1996), Partially molten middle crust beneath southern Tibet: Synthesis of project INDEPTH results, *Science*, *274*, 1684–1687.
- Ni, J., and M. Barazangi (1984), Seismotectonics of the Himalayan collision zone: Geometry of the underthrusting Indian plate beneath the Himalaya, *J. Geophys. Res.*, *89*, 1147–1163.
- Pandey, M., R. Tandukar, J. Avouac, J. Lave, and J. Massot (1995), Interseismic strain accumulation on the Himalayan crustal ramp (Nepal), *Geophys. Res. Lett.*, *22*, 751–754.
- Parrish, R., and K. Hodges (1996), Isotopic constraints on the age and provenance of the Lesser and Greater Himalayan sequences, *Geol. Soc. Am. Bull.*, *108*, 904–911.
- Paul, J., et al. (2001), The motion and active deformation of India, *Geophys. Res. Lett.*, *28*, 647–650.
- Pearson, O. N., and P. G. DeCelles (2005), Structural geology and regional tectonic significance of the Ramgarh thrust, Himalayan fold-thrust belt of Nepal, *Tectonics*, *24*, TC4008, doi:10.1029/2003TC001617.
- Pinet, C. (1992), Structure thermique et evolution des continents: Thermal structure and evolution of the continents, Doctoral thesis, Univ. de Paris VII, Paris.
- Pollack, H. N. (1965), Steady heat conduction in layered mediums: The half-space and sphere, *J. Geophys. Res.*, *70*, 5645–5648.
- Powell, C. M., and P. J. Conaghan (1973), Plate tectonics and the Himalayas, *Earth Planet. Sci. Lett.*, *20*, 1–12.
- Ratschbacher, L., W. Frisch, G. Liu, and C. Chen (1994), Distributed deformation in southern and western Tibet during and after the India-Asia collision, *J. Geophys. Res.*, *99*, 19,917–19,945.
- Raymo, M. E., W. F. Ruddiman, and P. N. Froelich (1988), Influence of late Cenozoic mountain building on ocean geochemical cycles, *Geology*, *16*, 649–653.
- Reiners, P. W., Z. Zhou, T. A. Ehlers, C. Xu, M. T. Brandon, R. A. Donelick, and S. Nicolescu (2003), Post-orogenic evolution of the Dabie Shan, eastern China, from (U-Th)/He and fission-track dating, *Am. J. Sci.*, *303*, 489–518.
- Ruddiman, W. F., and J. E. Kutzbach (1989), Forcing of the late Cenozoic northern hemisphere climate by plateau uplift in southeast Asia and the American southwest, *J. Geophys. Res.*, *94*, 18,409–18,427.
- Ruhl, K. W., and K. V. Hodges (2005), The use of detrital mineral cooling ages to evaluate steady-state assumptions in active orogens: An example from the central Nepalese Himalaya, *Tectonics*, *24*, TC4015, doi:10.1029/2004TC001712.
- Schatz, J. F., and G. Simmons (1972), Thermal conductivity of Earth materials at high temperatures, *J. Geophys. Res.*, *77*, 6966–6983.
- Schelling, D. (1992), The tectonostratigraphy and structure of the eastern Nepal Himalaya, *Tectonics*, *11*, 925–943.
- Schelling, D., and K. Arita (1991), Thrust tectonics, crustal shortening, and the structure of the far-eastern Nepal Himalaya, *Tectonics*, *10*, 851–862.
- Searle, M. P. (1996), Cooling history, erosion, exhumation, and kinematics of the Himalaya-Karakoram-Tibet orogenic belt, in *Asian Tectonics*, edited by A. Yin and M. A. Harrison, pp. 110–137, Cambridge Univ. Press, New York.
- Searle, M. P., and L. Godin (2003), The South Tibetan detachment and the Manaslu leucogranite: A structural reinterpretation and restoration of the Annapurna-Manaslu Himalaya, Nepal, *J. Geol.*, *111*, 506–523.
- Seeber, L., and V. Gornitz (1983), River profiles along the Himalayan arc as indicators of active tectonics, *Tectonophysics*, *92*, 335–367.
- Seeber, L., J. G. Armbruster, and R. C. Quittmeyer (1981), Seismicity and continental subduction in the Himalayan arc, in *Zagros, Hindu Kush, Himalaya Geodynamic Evolution, Geodyn. Ser.*, vol. 3, edited by H. K. Gupta and F. M. Delaney, pp. 215–242, AGU, Washington, D. C.
- Sobel, E. R., G. E. Hilley, and M. R. Strecker (2003), Formation of internally drained contractional basins by aridity-limited bedrock incision, *J. Geophys. Res.*, *108*(B7), 2344, doi:10.1029/2002JB001883.
- Spotila, J. A., K. A. Farley, and K. Sieh (1998), Uplift and erosion of the San Bernardino Mountains associated with transpression along the San Andreas fault, California, as constrained by radiogenic helium thermochronometry, *Tectonics*, *17*, 360–378.
- Stock, J. D., and D. R. Montgomery (1996), Estimating palaeorelief from detrital mineral age ranges, *Basin Res.*, *8*(3), 317–328.
- Stüwe, K., L. White, and R. Brown (1994), The influence of eroding topography on steady-state isotherms: Application to fission track analysis, *Earth Planet. Sci. Lett.*, *124*, 63–74.
- Suppe, J. (1983), Geometry and kinematics of fault-bend folding, *Am. J. Sci.*, *283*, 684–721.
- Tapponnier, P., G. Peltzer, and R. Armijo (1986), On the mechanics of the collision between India and Asia, in *Collision Tectonics*, edited by M. P. Coward and A. C. Ries, *Geol. Soc. Spec. Publ.*, *19*, 115–157.
- Tapponnier, P., G. Peltzer, A. Y. Ledain, R. Armijo, and P. Cobbold (1982), Propagating extrusion tectonics in Asia: New insights from simple experiments in plasticine, *Geology*, *10*, 611–616.
- Tapponnier, P., Z. Xu, F. Roger, B. Meyer, N. Arnaud, G. Wittlinger, and J. Yang (2001), Oblique stepwise rise and growth of the Tibetan Plateau, *Science*, *294*, 1671–1677.
- Wang, Q., et al. (2001), Present-day crustal deformation in China constrained by Global Positioning System measurements, *Science*, *294*, 574–577.
- Wesnousky, S. G., S. Kumar, R. Mohindra, and V. C. Thakur (1999), Uplift and convergence along the Himalayan frontal thrust of India, *Tectonics*, *18*, 967–976.
- Whipple, K. X., and G. E. Tucker (1999), Dynamics of the stream-power river incision model; implications for height limits of mountain ranges, landscape response timescales, and research needs, *J. Geophys. Res.*, *104*, 17,661–17,674.
- White, N. M., M. Pringle, E. Garzanti, M. Bickle, Y. Najman, H. Chapman, and P. Friend (2002), Constraints on the exhumation and erosion of the High Himalayan Slab, NW India, from foreland basin deposits, *Earth Planet. Sci. Lett.*, *195*, 29–44.
- Willett, S. D. (1999), Orogeny and orography; the effects of erosion on the structure of mountain belts, *J. Geophys. Res.*, *104*, 28,957–28,982.
- Willett, S. D., and M. T. Brandon (2002), On steady states in mountain belts, *Geology*, *30*, 175–178.
- Willett, S. D., R. Slingerland, and N. Hovius (2001), Uplift, shortening, and steady state topography in active mountain belts, *Am. J. Sci.*, *301*, 455–485.
- Willett, S. D., D. Fisher, C. Fuller, E.-C. Yeh, and C.-Y. Lu (2003), Erosion rates and orogenic-wedge kinematics in Taiwan inferred from fission-track thermochronometry, *Geology*, *31*, 945–948.
- Wobus, C. W., K. V. Hodges, and K. X. Whipple (2003), Has focused denudation sustained active thrusting at the Himalayan topographic front?, *Geology*, *31*, 861–864.
- Wobus, C., A. Heimsath, K. X. Whipple, and K. V. Hodges (2005), Active surface thrust faulting in the central Nepalese Himalaya, *Nature*, *434*, 1008–1011.
- Yin, A., and T. M. Harrison (2000), Geologic evolution of the Himalayan-Tibetan orogen, *Annu. Rev. Earth Planet. Sci.*, *28*, 211–280.
- Zhang, P., P. Molnar, and W. R. Downs (2001), Increased sedimentation rates and grain sizes 2–4 Myr ago due to the influence of climate change on erosion rates, *Nature*, *410*, 891–897.

I. D. Brewer, Department of Geosciences, Pennsylvania State University, University Park, PA 16802, USA. (dr\_i\_brewer@hotmail.com)

D. W. Burbank, Department of Earth Science, University of California, Mail Code 1100, 1140 Girvetz Hall, Santa Barbara, CA 93106, USA. (burbank@crustal.ucsb.edu)